An in-depth view of the mid-infrared properties of point sources and the diffuse ISM in the SMC giant HII region, N66

Journal Item

An In-Depth View of the Mid-Infrared Properties of Point Sources and the Diffuse ISM in the SMC Giant HII Region, N66

David G. Whelan

Department of Astronomy, University of Virginia, P.O. Box 400325, Charlottesville, VA 22904

dww7v@astro.virginia.edu

Vianney Lebouteiller

Laboratoire AIM, CEA, Université Paris Diderot, IRFU/Service d'Astrophysique, Bât. 709, 91191 Gif-sur-Yvette, France

vianney.lebouteiller@cea.fr

Frédéric Galliano

Service d'Astrophysique - Laboratoire AIM, CEA/Saclay, L'Orme des Merisiers, 91191 Gif-sur-Yvette, France

frederic.galliano@cea.fr

Els Peeters[1]

Department of Physics & Astronomy, University of Western Ontario, 1151 Richmond Street, London, ON N6A 3K7, Canada

epeeters@uwo.ca

Jeronimo Bernard-Salas[2]

IAS, Université Paris-Sud 11, Bat. 121, 91405 Orsay, France

jeronimo.bernard-salas@ias.u-psud.fr

Kelsey E. Johnson[3]

Department of Astronomy, University of Virginia, P.O. Box 400325, Charlottesville, VA 22904

kej7a@virginia.edu

Rémy Indebetouw[4]

Department of Astronomy, University of Virginia, P.O. Box 400325, Charlottesville, VA 22904

ri3e@virginia.edu

and

Bernhard R. Brandl

Leiden Observatory, Leiden University, P.O. Box 9513, 2300 RA Leiden, The Netherlands

brandl@strw.leidenuniv.nl

Received _____; accepted _____

[1]SETI Institute, 189 Bernardo Avenue, Suite 100, Mountain View, CA 94043, USA

[2]Department of Physical Sciences, Open University, Milton Keynes, MK7 6AA, UK

[3]Adjunct at National Radio Astronomy Observatory, 520 Edgemont Road, Charlottesville, VA 22904, USA

[4]Assistant Staff Scientist, National Radio Astronomy Observatory, Charlottesville, VA 22904, USA

ABSTRACT

The focus of this work is to study mid-infrared point sources and the diffuse interstellar medium (ISM) in the low-metallicity (~ 0.2 $Z_\odot$) giant HII region N66 in order to determine properties that may shed light on star formation in these conditions. Using the *Spitzer Space Telescope*'s Infrared Spectrograph, we study polycyclic aromatic hydrocarbon (PAH), dust continuum, silicate, and ionic line emission from 14 targeted infrared point sources as well as spectra of the diffuse ISM that is representative of both the photodissociation regions (PDRs) and the HII regions. Among the point source spectra, we spectroscopically confirm that the brightest mid-infrared point source is a massive embedded young stellar object, we detect silicates in emission associated with two young stellar clusters, and we observe spectral features of a known B[e] supergiant that are more commonly associated with Herbig Be stars. In the diffuse ISM, we provide additional evidence that the very small grain population is being photodestroyed in the hard radiation field. The 11.3 μm PAH complex emission exhibits an unexplained centroid shift in both the point source and ISM spectra that should be investigated at higher signal-to-noise and resolution. Unlike studies of other regions, the 6.2 μm and 7.7 μm band fluxes are decoupled; the data points cover a large range of $I_{7.7}/I_{11.3}$ PAH ratio values within a narrow band of $I_{6.2}/I_{11.3}$ ratio values. Furthermore, there is a spread in PAH ionization, being more neutral in the dense PDR where the radiation field is relatively soft, but ionized in the diffuse ISM/PDR. By contrast, the PAH size distribution appears to be independent of local ionization state. Important to unresolved studies of extragalactic low-metallicity star-forming regions, we find that emission from the infrared-bright point sources accounts for only 20-35% of the PAH emission from the entire region. These results make a comparative dataset to other star-forming regions

with similarly hard and strong radiation fields.

Subject headings: stars: formation – infrared: ISM – ISM: lines and bands – ISM: molecules – ISM: HII region – ISM: dust

1. INTRODUCTION

The Small Magellanic Cloud (SMC) is an excellent test-bed for studying star formation in a low-metallicity environment. Its low metallicity (~ 0.2 $Z_\odot$ determined from numerous elemental abundances; Russell & Dopita 1992) and strong interstellar radiation field (ISRF; 4-10 G_0, Cox et al. 2007) make it an important contrasting environment to star forming environments in the Milky Way or the Large Magellanic Cloud (LMC). The SMC is also a good comparative theater to studies of 'passive' star formation in blue compact dwarf galaxies (BCDs; see Thuan 2008, for the distinction between "active" and "passive"), because their star-forming regions have similar densities (~ 100 cm^{-3}), star formation rates (~ 0.1 $M_\odot$ yr^{-1}), radiation field hardnesses, and the SMC is the lowest-metallicity nearby star-forming region (Wilke et al. 2004; Madden et al. 2006).

N66 (Henize 1956) is the largest HII region in the SMC, covering an area on the sky of approximately $180'' \times 300''$, and therefore offers the best view of large-scale star formation in the SMC. It surrounds a large stellar association known as NGC 346. N66 contains 33 O stars distributed across the HII region, which is about half the number for the entire SMC, and 11 of them are earlier than type O7 (Massey, Parker, & Garmany 1989). The most massive star is of O3III(f*) (~ 100 $M_\odot$) or O3vf* (~ 90 $M_\odot$) type (Walborn & Blades 1986; Massey et al. 2005). The O stars illuminate the surrounding ISM and are responsible for an Hα luminosity of about 60 times that of the Orion nebula (Kennicutt 1984). UV and optical spectra have been used to derive an age of about 3 Myr for the O stars in N66 and a metallicity of 0.2 $Z_\odot$ (the metallicity has been determined independently for individual O stars, forbidden line emission originating in the gas, and spectral models; Haser et al. 1998; Lebouteiller et al. 2008; Bouret et al. 2003).

N66 is experiencing ongoing star formation. Simon et al. (2007) identified about 100 embedded YSOs with *Spitzer* IRAC and MIPS photometry, and Gouliermis et al. (2010)

found a further 263 candidate young stellar sources including intermediate mass pre-main sequence and Herbig AeBe stars, as well as massive YSO candidates. The first mid-IR study of N66, with ISOCAM, showed strong nebular [SIV] 10.51 μm and [NeIII] 15.56 μm emission across the region that is indicative of young and massive (O- and B-type) stars, the presence of faint polycyclic aromatic hydrocarbon (PAH) emission bands, a mid-infrared continuum from very small grain (VSGs) and large thermal dust grain emission, and an ISRF at 1600 Å $\geq 10^5$ times that of solar (Contursi et al. 2000). A companion paper to Contursi et al., Rubio et al. (2000), included [OIII] λ5007, H_2 v(1-0) S(1) 2.12 μm, and CO observations to show that the peaks in H_2, CO, and PAH emission are all spatially correlated across the photodissociation regions (PDRs) in general, and further suggested that the CO has been largely photodissociated across the HII region by the O star population, and exists only in small clumps. Sandstrom et al. (2012) included N66 as part of a study of PAHs in HII regions across the SMC, and determined that the PAH population is both smaller and less ionized than in higher-metallicity galaxies. In two comparison studies, the atomic/ionic gas content and the effects of metallicity on PAH emission were studied for N66, 30 Doradus in the LMC, and NGC 3603 in the Milky Way (Lebouteiller et al. 2008, 2011). The elemental abundances were determined for each region using the ionic forbidden lines from mid-infrared spectra; for N66, the results confirmed that the metallicity is about 0.2 $Z_\odot$. It was discovered that the PAHs are photodestroyed in radiation fields where nebular [NeIII]/[NeII] $\gtrsim 3$, and that this photodestruction law is independent of metallicity. What is still unclear about N66 is where the PAH emission originates, and what conditions are traced by the PAH emission. In particular, PAH ionization state, which is a function of the ultraviolet (UV) radiation field, is also equally sensitive to electron density (charge state $Z \propto G_0 T^{1/2}/n_e$; Tielens 2005), and there are cases evident in the literature that suggest that neutral PAHs have the ability to exist inside HII regions (e.g. in the vicinity of the Horsehead Nebula: Compiègne et al. 2007).

The reason that star formation is often traced by emission from PAHs (Peeters et al. 2004) is that, while PAHs are sensitive to excitation from a broad range of wavelengths (UV-IR), they are particularly susceptible to excitation by UV photons. PAH emission is commonly observed in the PDRs around young massive clusters (Léger & Puget 1984; Tielens et al. 1999). These spectral features are predominantly present from 3-17 μm. The molecules responsible for this emission are typically dozens to thousands of carbon atoms large. Following photoexcitation, they emit by fluorescence from stretching and bending modes either from the carbon-to-hydrogen (C-H) or carbon-to-carbon (C-C) bonds.

Due to the stochastic excitation and emission mechanism as well as the ionization balance of PAHs, the local physical conditions have a large impact on the observed PAH band ratios via radiation field hardness, column density, dust temperature, and dust composition (Hony et al. 2001; Peeters et al. 2002). Due to the relatively low ionization potentials of PAHs (about 6-8 eV for small PAHs; Tielens 2005, Table 6.1), PDRs are expected to be dominated by ionized PAHs whereas regions with weaker radiation fields, such as the diffuse ISM in the Milky Way or inside molecular clouds, should have largely neutral or negatively-charged PAHs (Bakes & Tielens 1994).

In order to study the mid-infrared properties of N66 in greater detail with particular emphasis on the PAH emission as an independent tracer of the physical conditions across the region, we present *Spitzer Space Telescope*/IRS spectra of a number of infrared point sources and use the spectral information along the entire IRS long slits to study the dust and gas emission throughout the HII region and photodissociation region (PDR). We present the observations in Section 2, describe our data reduction in Section 3, present our analysis in Section 4, and summarize the results in Section 5.

2. OBSERVATIONS

N66 (Figure 1) was observed as part of the IRS GTO program to study massive star formation in giant HII regions in the Local Group (PID 63). Imaging using *Spitzer*/IRAC (Fazio et al. 2004) of the whole region revealed a number of bright point sources, the brightest eight of which were chosen for spectroscopic follow-up with the low- and high-resolution modules of the *Spitzer* Infrared Spectrograph (IRS; Houck et al. 2004). The present study concentrates on the short-wavelength low-resolution spectra only ($\lambda < 14.7$ μm); the high-resolution *Spitzer* spectra have been analysed in Lebouteiller et al. (2008, 2011) to determine element abundances and to constrain the strength of the interstellar radiation field (ISRF) using forbidden emission lines, and the long-wavelngth low-resolution data (15 μm $< \lambda <$ 37 μm) have not been included due to the spatial resolution and slit orientation mismatch. This dataset is therefore in contrast to that presented in Sandstrom et al. (2012), in which long- and short-wavelength spectral maps are used to analyze N66. While they analyzed full spectral maps of the entire region, the data we present here is deeper and allows us to study the faint extended emission around the point sources at a level of detail that the full maps did not allow.

The pointings for the original eight positions (Astronomy Observing Request 4385024) were systematically offset by about 5″ with respect to the actual source positions. As a result, most of the intended point sources were partially or wholly outside of the 3.6″-wide slit. However, there is at least one point source in each of these slits regardless, though they are not always the intended ones. In order to target the intended point sources, N66 was re-observed with correct astrometry (AOR 16207872). The point sources detected in the original and re-observed samples are shown in Figure 2 along with the slit orientations. See Table 1 for a full list of the point source (PS) positions, labeled in order of decreasing right ascension, and Table 2 for a list of slit centroids.

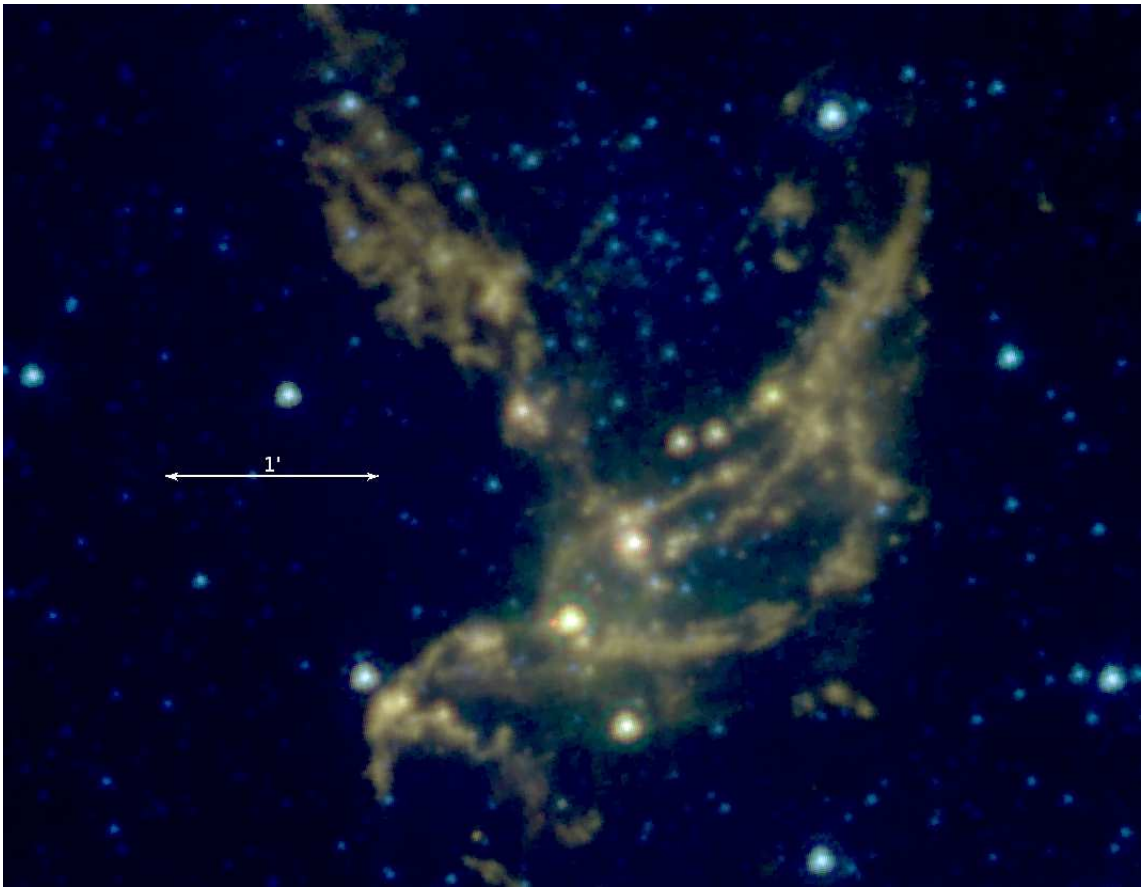

Fig. 1.— A *Spitzer*/IRAC 3-color image of N66. Blue is 3.6 μm, green is 5.8 μm, and red is 8.0 μm. The 5.8 μm and 8.0 μm images trace the PAH emission in the region, highlighting the PDRs, while the 3.6 μm image traces the stellar population; in particular, the old star cluster, BS 90, is visible to the north of NGC 346. The angular scale of 1 $'$ corresponds to a physical distance of 17.6 pc at the distance of NGC 346.

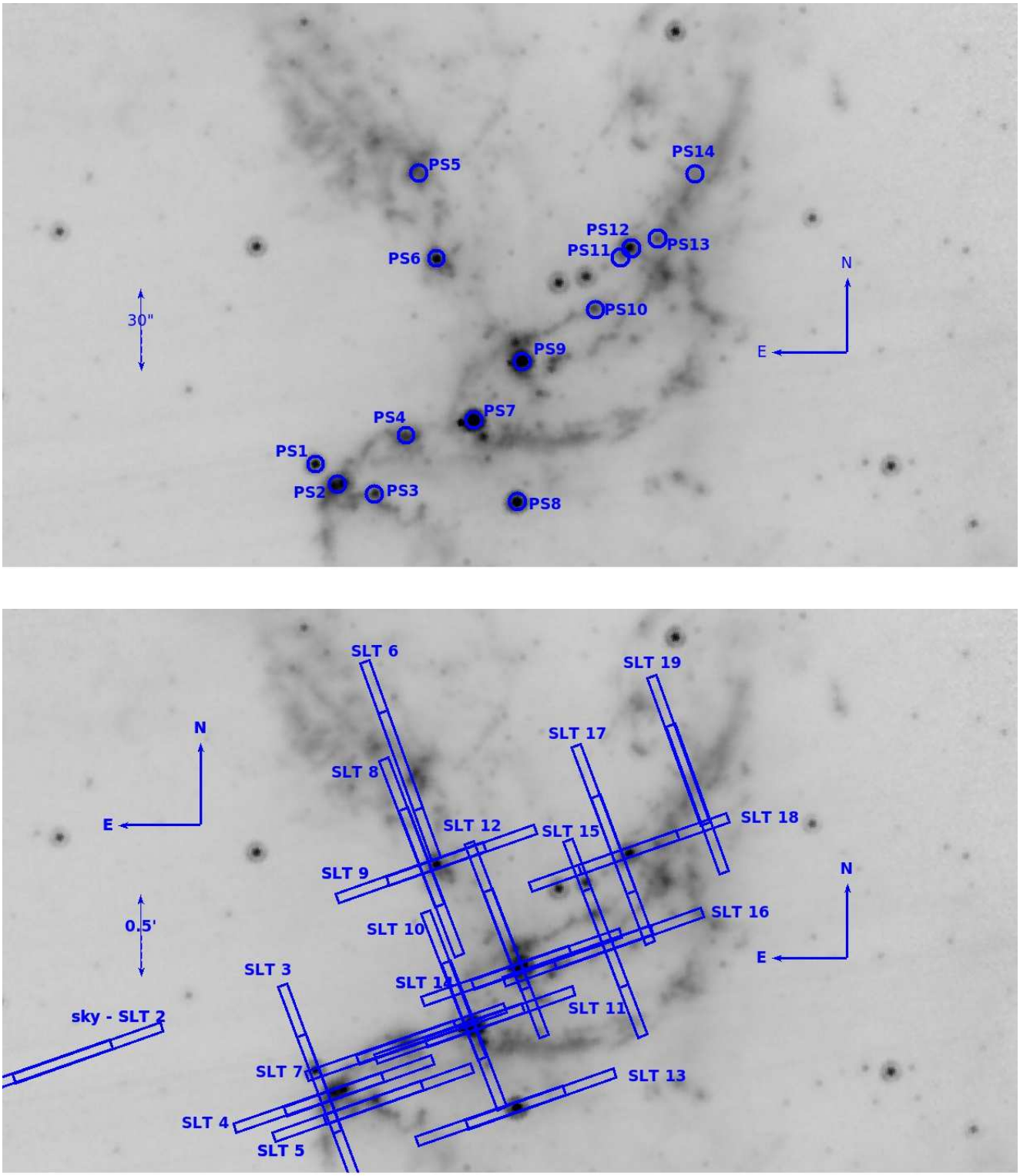

Fig. 2.— The *IRAC* 8.0 μm image with the observed point sources circled and labeled in blue, and the labeled slit positions across the region. See Tables 1 and 2 for coordinate information.

Three exposures were taken at each nod position in staring mode (see the *Spitzer/IRS* manual), where the source is positioned at 1/3 (nod1) and 2/3 (nod2) of the slit length. The original observations had 60-second exposure times, whereas the re-observed sample have 15-second exposure times.

The low-resolution spectra ($\lambda/\Delta\lambda \sim$ 65-130) cover the spectral range 5.2-14.7 μm using the short-low (SL) module. The SL-1 slit covers the spectral range 7.4-14.7 μm and the SL-2 slit covers the spectral range 5.2-7.7 μm. The sizes of the two slits ($3.7'' \times 57''$ and $3.6'' \times 57''$ respectively) correspond to a physical size of 1.1 × 16.7 pc at the distance of N66 (we adopt a value of 60.6 kpc from Hilditch et al. 2005). Therefore the point sources, with a FWHM at 6 μm of 4 pixels out of 34, are resolved down to about 2 pc along the slit.

3. DATA REDUCTION

3.1. Spitzer/IRS Image Reduction

The *Spitzer/IRS* images were processed with the *Spitzer Science Center (SSC)* pipeline, version S18.7. The basic calibrated data (BCD) were used. Images were cleaned by interpolating values over flagged bad pixels using the *SSC*-provided IDL package IRSCLEAN[1]. After cleaning, the observed sky positions were subtracted from the other positions in their respective AORs to remove any intervening flux from zodiacal light, the Milky Way, and foreground SMC. Since the sky positions are relatively far from N66, we may assume that emission in the sky spectra is primarily from the diffuse SMC and not from N66. The spectra of these sky positions exhibit [SIV] emission but no dust features. The strength of the sky position's [SIV] emission is 7.9×10^{-21} W cm^{-2}, which is almost 50% the value for the lowest [SIV] flux found in the extended emission spectra (see § 3.2),

[1]All *SSC*-provided packages may be found at *http* : *//irsa.ipac.caltech.edu/data/SPITZER/docs/data*

and less than 20% of the flux for the rest of the spectra.

3.2. Spectral Extractions

Using the optimal extraction routines available in the *Spectroscopy Modeling Analysis and Reduction Tool* (SMART-AdOpt; Lebouteiller et al. 2010; Higdon et al. 2004), point source and extended emission can be simultaneously extracted. SMART's optimal extraction routines fit a polynomial function to the extended emission as well as template supersampled point spread functions (PSFs) to point sources in the slit, as shown in Figure 3. The backgrounds are relatively smooth for these spectra, and polynomials of four orders and less were used. Details, including how to fit partially extended point sources and measuring the residuals, are presented in Lebouteiller et al. (2010). However, the fundamental operation demands that for each wavelength element, the relative weights to the total flux assigned to the point source(s) and background are measured simultaneously. Therefore, the flux is distributed to each component in a way that agrees with the combination of point source(s) and polynomially-fitted background.

The advantage of simultaneous point source and extended emission extraction compared to more traditional, variable column extractions is illustrated in Figure 4. Two point sources have been extracted using two different methods as an example. The source in the left-hand plot is a massive embedded young stellar object (YSO), PS7, and the right-hand plot shows the spectrum of the unresolved dust emission associated with the young star cluster NGC 346, PS9. The 'column extraction' extracts all of the emission inside a column that varies in width with the PSF. The 'optimal extraction' uses the SMART-AdOpt routines. There are significant differences revealed by the optimal extraction method. For example, the [SIV] 10.51 μm emission line, which is often prominent in HII regions, is not associated with the point source spectra; the reason it appears in the column extraction is because it is

nebular emission along the line-of-sight to the point source. In fact, we would get the wrong diagnostic with a variable column extraction, since the nebular [SIV] would be erroneously assigned to the point source. The [NeII] 12.81 μm emission line is also nebular in nature for the massive embedded YSO (left-hand plot). In addition to the nebular forbidden atomic lines, a certain amount of the dust continuum is also missing from the optimally extracted spectra, meaning that it is also nebular in nature. By separating out the point source from the line-of-sight nebular emission, we have separate views of emission that is associated with the unresolved point sources in N66 and emission that originates in the diffuse HII region and PDR.

Optimal extraction of all of the pointings was performed, producing point source and extended emission spectra from the full slit length for each pointing. Two of the re-observed pointings have extended emission spectra that were dominated by noise and are not used in the analysis.

Observations where the point source lies partially outside of the slit in the dispersion direction were extracted with a special tool developed for and included in SMART-AdOpt. Applying the centered PSF template to an observation with incorrect pointing makes the spectral shape incorrect, but accounting for the pointing error allows a properly-shaped PSF to be fit to the point source so that regular optimal extraction and accurate flux calibration can be done. For details on the source extraction for sources offset in the dispersion direction, see Lebouteiller et al. (2010). The reduced spectra are shown in Appendix 1 at the end of this paper.

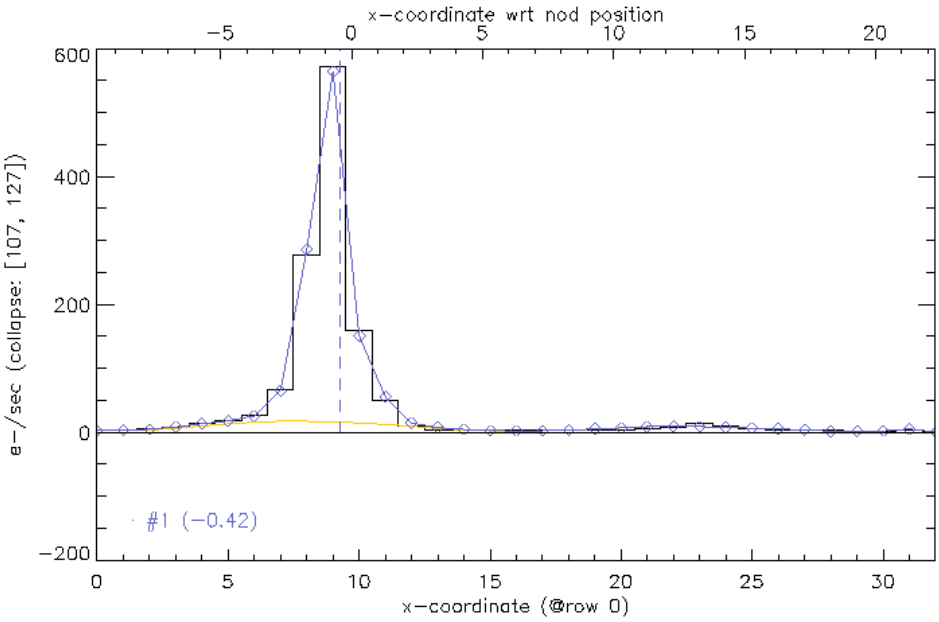

Fig. 3.— The spatial extent of an extracted point source and the underlying extended emission for the 7-9 μm continuum as output by SMART-AdOpt. The yellow line is a polynomial fit to the background emission in the slit and a stellar template is used to fit the point source emission. The IRS data are shown in black histogram. The point source is labeled, as would other point sources found, at the bottom of the plot, along with its centroid in pixels with respect to the nod position (on top of the plot) and with respect to the edge of the slit (bottom of the plot).

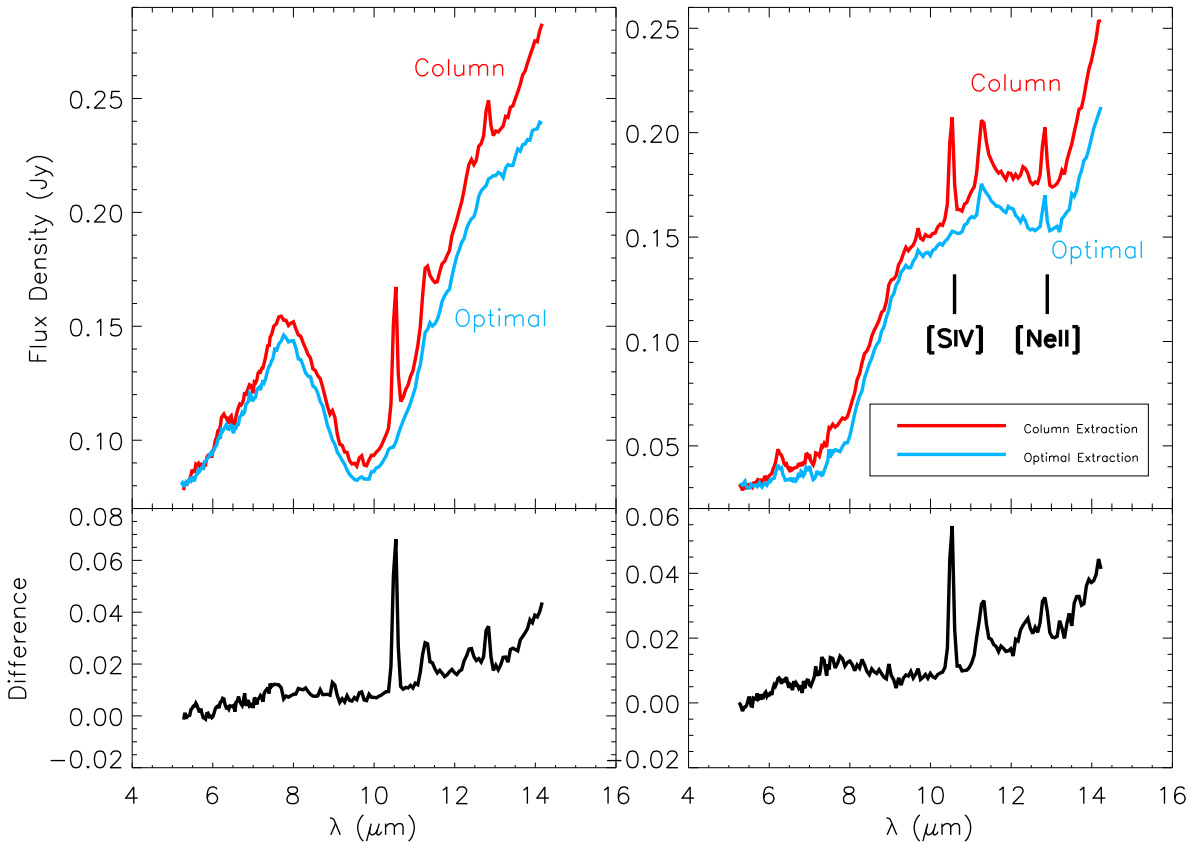

Fig. 4.— Variable column extractions (in red) are shown overplotted with optimal point source extractions (in blue) for the two brightest IR point sources in N66: the massive YSO in N66A (left, PS7) and NGC 346 (right, PS9). The column extractions include a significant amount of emission along the line-of-sight that is not associated with the point source: the [SIV] 10.51 μm emission, a portion of the [NeII] 12.81 μm emission, and some dust continuum emission is not associated with these point source spectra, but is nebular in nature. This nebular emission is shown in the "Difference" spectra in the bottom panels.

3.3. Spectral Decomposition

Typical mid-infrared spectra of HII regions and their surrounding PDRs have the following features: a dust continuum, several prominent PAH features, molecular hydrogen emission lines, atomic and ionic emission lines, and absorption or emission features due to small silicaceous grains centered at 9.8 μm and 17 μm. In order to study the dust and gas diagnostics in N66, all of the spectra were decomposed into these components.

We used the specral decomposition tool PAHFIT (Smith et al. 2007). PAHFIT models the dust continuum that underlies the PAH features with as many as eight blackbody continua at fixed temperatures less than 300 K, fits the silicate absorption features at 9.8 μm and 17 μm, and models the PAH features with asymmetric Drude profiles. In order to fit the spectra for N66 with PAHFIT, a couple of small changes were made. In some cases, the input full-width at half maxima (FWHM) of the 6.2 μm and 11.3 μm features needed to be changed in order to fit the features more precisely (see § 4.3 below for a discussion about the 11.3 μm PAH feature profiles). Second, for sources that exhibit a silicate emission feature, two additional Drude profiles were added to model the 9.8 μm silicate emission feature: these Drude profiles, centered at 9.2 μm and 10.0 μm, have FWHM of 0.3 μm and 0.2 μm respectively. For spectra with silicate emission features included, PAHFIT did *not* also fit silicate absorption features. Due to the presence of Hydrogen recombination lines in some of the spectra, we include the HI 6-5 7.46 μm line to PAHFIT's line list. Example point source and extended emission PAHFIT fits are shown in the top panels of Figure 5, where the plotting scheme is explained in the caption. One major difference in the fits between the point source and extended emission spectra is that the silicate absorption feature is only fit to those point source spectra that do not explicitly require a silicate emission feature, and none of the extended emission features exhibit silicate absorption in the final fits.

There is some concern that PAH fitting routines like PAHFIT may be introducing

errors inadvertently into the PAH fluxes. When applying PAHFIT, the underlying PAH "plateaux" are incorporated into the wings of the Drude profiles used to fit the PAH bands, in particular for the 7.7 μm band. Peeters et al. (2013, in preparation) has found that the spatial morphology of the plateau is quite distinct from that of the 6.2, 7.7, and 8.6 μm PAH bands in data of the reflection nebula NGC 2023. To see if the PAH plateaux in the N66 spectra is also decoupled from the PAH features, we have fit a spline to the underlying continuum and measured the PAH features above the continuum, as in Galliano et al. (2008b). We have determined that, although the exact values for the PAH band fluxes differ depending on the decomposition method used, the trends discussed in detail in § 4.5 hold regardless. The spectral decomposition method illustrated in Figure 5 is a reliable method for comparing PAH band fluxes.

Due to concerns about error propagation from extraction to decomposition, the errors of the PAH feature strengths were determined with a Monte Carlo method. The root mean square error in the continuum near 6 μm was measured for each spectrum and then used to randomly perturb the spectrum. 6 μm was chosen because the noise is systematically higher at the shortest wavelengths in the SL spectrum, due to the lower signal in these sources at this wavelength. The noise is, on average, two times greater at 6 μm than it is at 14 μm, measured as the standard deviation of the root mean square of the difference of the unperturbed spectrum and the best fit PAHFIT model. The spectrum, including the random noise, was then fit with PAHFIT and the resultant strengths of the PAH features were recorded. This was done 300 times, after which the standard deviation of the PAH feature strength measurements was taken as the statistical error in the 300 fitted feature strengths.

While PAHFIT also fits any number of user-requested atomic, ionic, and molecular features in addition to the dust continuum and PAH features, we fit the narrow lines

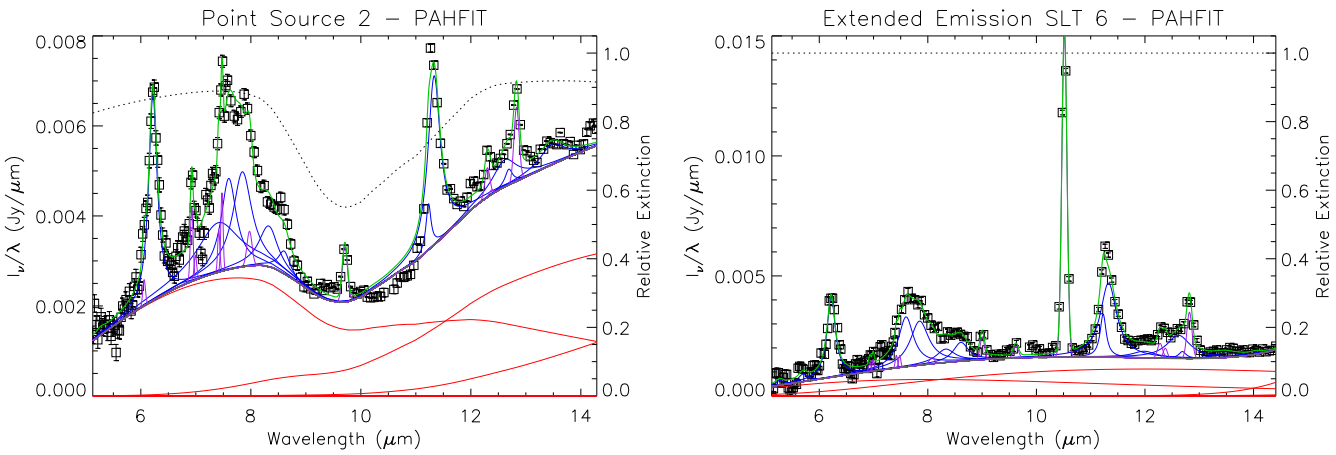

Fig. 5.— Example spectral fits with PAHFIT are shown for two sources, point source PS2 and the extended emission spectrum SLT6. The red lines are blackbody fits to the dust continuum, the blue features are PAHs, the narrow features in purple are atomic and molecular emission lines, the dotted line is the relative extinction and the green line is the composite fit to the data (squares).

manually with the IDEA tool in SMART. The reason for this additional step is that PAHFIT functions first and foremost as a fitting tool, and will therefore include all of the parameters it is given into the final solution. This means that in the point source spectra, for instance, PAHFIT will generally give the [SiV] 10.51 μm line a flux even when it is clear from a visual inspection that this line is not detected. Therefore, in order to systematically determine narrow line fluxes and upper limits, we chose to use a manual tool for line fits. We used a first-order local continuum subtraction to estimate continuum flux beneath the narrow features. The [NeII] 12.81 μm feature is blended with a PAH feature and the line flux may therefore contain some PAH emission; due to the presence of PAHs in all spectra, we believe that any offset due to this contamination is largely systematic but may contribute substantially to the point source spectra PS12, PS13, and PS14, which exhibit much lower [NeII] fluxes than the other spectra. The continuum at 13.7-14.2 μm contains two prominent PAH features that, when compared to the PAHFIT dust continuum and PAH feature fits, systematically contributed roughly twenty per-cent to the continuum at these wavelengths; the continuum was therefore measured as the average in the PAHFIT dust continuum beneath the PAH features. The final atomic, ionic, PAH, and continuum measurements along with their errors are given in Tables 3 & 4.

4. ANALYSIS

4.1. Point Source Identification

We carried out a literature search in order to identify known objects associated with the infrared point source centroids. Table 1 lists the targeted point sources from this study, corresponding labels from Lebouteiller et al. (2008) and Contursi et al. (2000), and additional information from the literature. All point sources are identified as sites of recent or ongoing star formation, and are typically young protostars or young stellar clusters. A

number of the point sources exhibit interesting spectral features that are worth a closer look. We describe these point sources in detail below.

4.1.1. Young Star Clusters Exhibiting Silicates in Emission

Unresolved emission from two bright star clusters in N66 exhibit silicate emission features in their spectra: NGC 346 (PS9) and N66B (PS6); see Figure 6. Both of these point sources are bright Hα sources (Henize 1956), contain 'blue' stars (Massey, Parker, & Garmany 1989; Gouliermis et al. 2006), and have been modeled as $\sim$ 3 Myr old with *Hubble* color-magnitude diagrams (Sabbi et al. 2007). This age is consistent with the presence of remnant dust from the natal cloud surrounding the cluster.

The origin of the silicate emission is most likely an optically thin layer of intracluster and/or enveloping dust that has been heated to $\sim$ 200 K by the stars in the central clusters. The presence of silicate emission suggests a relatively low optical depth; this is supported by optical data of N66 (see, for example, the high-resolution *Hubble* data presented in Sabbi et al. 2007), where the stars in the centers of the clusters are clearly visible through the intervening dust, and supported by the measured extinction by dust (Caplan et al. 1996). This geometry is similar to clumpy model geometries for young star clusters presented in Whelan et al. (2011), where silicate emission/absorption was found to be dependent on the line-of-sight dust geometry. Neither cluster is resolved in the spectral slit, and we therefore did not employ the IRS LL module ($15 < \lambda < 37\mu$m) to measure the 17 μm silicate emission as in Hao et al. (2005) and Sturm et al. (2005) because the flux mis-match between the SL and LL *Spitzer*/IRS modules is very substantial and would bias the silicate dust temperature measurement. The presence of an O5.5V star in N66B and an O9V star in NGC 346 means that the point source extractions show a little [SIV] emission in N66B, none in NGC 346, and [NeII] emission in both. The [SIV] emission in N66B is

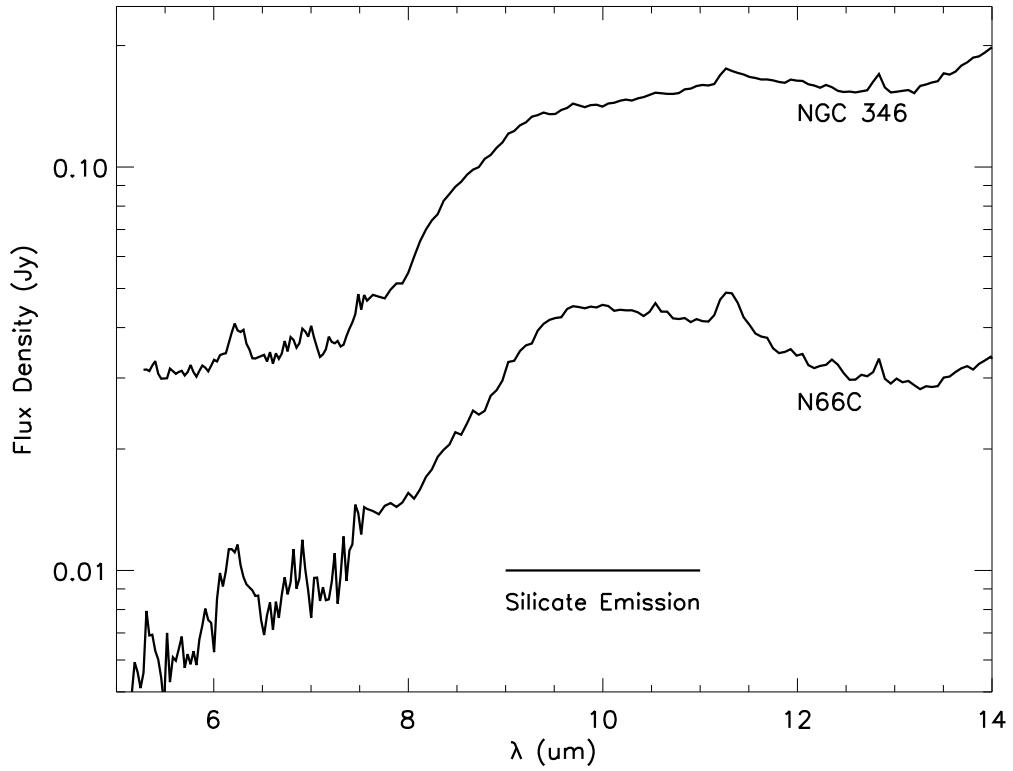

Fig. 6.— The spectra of two stellar clusters in the N66 giant HII region: NGC 346 (PS9), the central source and brightest optically visible cluster, and N66B (PS6), a large stellar cluster to the north of NGC 346 (see Figure 2). Both show pronounced silicate emission features.

likely due to the O5.5V star. See Sabbi et al. (2008), Figure 7 for a map of the positions of the known O stars across N66, many of which appear off of the stellar cluster positions.

Silicates in emission associated with young star clusters have not been observed regularly before. In NGC 3603, pointings on and near the central star cluster show silicate emission (Lebouteiller et al. 2007). There is one pointing in 30 Doradus in the LMC (source B; Indebetouw et al. 2009, and also found in Lebouteiller et al. 2008) near R136 that exhibits silicate emission, but this source has been spectroscopically identified as an M-type supergiant star (Parker 1993). While there are numerous detections of silicates in emission among protoplanetary systems (*e.g.* Furlan et al. 2011; Sicilia-Aguilar et al. 2007) and evolved stars such as asymptotic giant branch stars (AGBs, both galactically and extragalactically; see Sloan & Price 1995; Lebouteiller et al. 2012), there are relatively few young stellar clusters that show silicate emission. Robberto et al. (2005) show that a diffuse silicate population is likely across the Orion nebula. Compared with those observations, the silicate emission observed in NGC 3603, NGC 346, and N66B is distinct in that it is clearly associated with the stellar clusters and not visibly dispersed across the region. It seems likely that the strong silicate emission associated with the star clusters in N66 and NGC 3603 is tied to a relatively short period of time in the early evolution of star clusters and will only last a short period of time; that these clusters are definitively young (e.g. Gouliermis et al. 2006) and therefore contain no AGB stars excludes the possibility of silicate-rich winds from post-main sequence stars contributing to the observed silicate emission.

4.1.2. Silicate and PAH Emission Associated with a B[e] star

There is a third spectrum exhibiting a silicate emission feature: PS8. In this instance, the silicate feature is not as pronounced as for the star clusters discussed above, though

it has pronounced PAH features as well (see Figure 15 in the Appendix). Searching by position, we found a Be star at those coordinates, Cl* NGC 346 KWBBE 200. Wisniewski et al. (2007) fit a UV-to-8 μm spectral energy distribution (SED) with a B-star template and a T $\sim$ 800 K blackbody, observed P Cygni profiles on a number of optical spectral lines, roughly determined a luminosity of $10^{4.4}$ $L_{\odot}$, and concluded that this source is a B[e] supergiant. Evidence against it being a Herbig Be system is that no inverse P Cygni profiles associated with infall were observed, and that the derived luminosity is on the high end for Herbig Be stars. We note, however, that silicate emission and strong PAH bands are often detected in Herbig AeBe star systems (e.g. Keller et al. 2008), where cooler dust and PAHs are expected due to its young age. Additionally, PS8 exhibits a Class A PAH spectrum as shown in Figure 8 and discussed in § 4.3, which is typical for non-isolated Herbig AeBe stars (Peeters et al. 2002), and is a 24 μm source as observed by *Spitzer*/MIPS (Rieke et al. 2004), suggesting that there is cold dust that Wisniewski et al.'s SED fit did not account for. While the absence of inverse P Cygni profiles offers a conundrum, the evidence from the mid-IR suggests that KWBBE 200 is, in fact, a Herbig AeBe star, not a B[e] supergiant.

4.1.3. An Embedded Massive Young Stellar Object at the Edge of HII *Region N66A*

The single brightest mid-IR point source in N66, PS7, lying at the location of the HII region N66A (Henize 1956), was found to be a 16.6 $M_{\odot}$ class I young stellar object (YSO) by Simon et al. (2007) using *Spitzer/IRAC* and *MIPS* photometry matched to models of class I protostars presented in Robitaille et al. (2006). Shown in Figure 7, the spectrum has a deep silicate feature at 9.8 μm which corresponds to high optical depth and therefore supports the class I designation. Furthermore, the presence of H_2O ice in the 6-7.5 μm range and a CO_2 ice feature at 15 μm in the high-resolution *Spitzer* spectrum of N66A

suggests cold, dense conditions similar to other massive class I YSO environments (*e.g.* van Loon et al. 2005). Lastly, there is no [SIV] or [NeII] detected, suggesting that the central heating source does not have a strong UV continuum. These spectroscopic signatures all confirm Simon et al.'s original designation.

To confirm the YSO mass, we fit *Spitzer*/IRS data (wavelength coverage from 5 to 35 μm) with the Robitaille et al. models[2]. For these fits of an embedded protostar, stellar temperature (and mass), disk/envelope mass and inner/outer radii are all fit, though for embedded sources disk masses are known to be ill-constrained. The best fit to our data was a 17.8 $M_\odot$ YSO embedded in an envelope of about 10^3 $M_\odot$. The circumstellar extinction is calculated to be $A_V = 25.7$, and the interstellar extinction is $A_V = 0.1$. For comparison, $\tau_{9.8\mu\mathrm{m}}$=1.88 from the PAHFIT parameter fit to this source, which is consistent with the circumstellar extinction (Roche & Aitken 1985). The total luminosity of this model is 3.47×10^4 $L_\odot$. This result differs from the fit presented in Simon et al. (2007) by a $\sim 7\%$ increase in mass and $\sim 15\%$ increase in luminosity.

Heydari-Malayeri & Selier (2010) studied the *Hubble* data for the HII region N66A in great detail and determined that it is supported by an O8 star. While the massive YSO discussed in this section dominates the infrared emission, the fine structure emission in the extended emission spectrum is due to the young O- and B-star population in N66A, while the diffuse dust emission probably comes from the PDR at the interface to the molecular cloud in which the massive YSO is buried. There are in fact two YSOs at PS9's centroid in the Simon et al. (2007) atlas; the more massive YSO studied here dominates the infrared luminosity substantially: there is a factor of about 19 ratio between the luminosities of the two YSOs. At the sensitivity of these data, the massive YSO is the only point source

[2]We used the SED fitting routine described in Robitaille et al. (2007) and available to the public via: http://caravan.astro.wisc.edu/protostars/

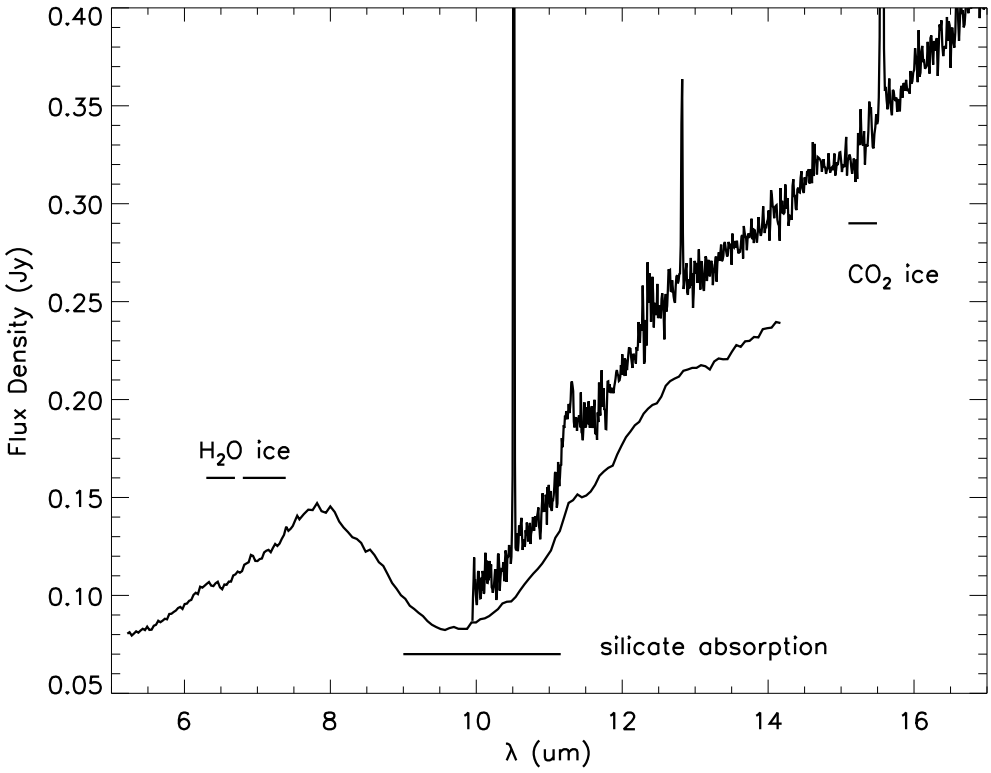

Fig. 7.— The *Spitzer/IRS* SL/SH spectrum of N66A exhibits features commonly associated with a massive young stellar object: water ice features between 6-7.5 μm, deep silicate absorption indicative of high optical depth, CO_2 ice at 15 μm, and a strong mid-infrared continuum. The nebular lines seen in the high-resolution spectrum come from intervening diffuse material.

detected.

4.2. Ionic Lines

Ionic emission lines in an HII region can help quantify the strength and hardness of the radiation (see Lebouteiller et al. 2011) but may also be used to shed light on the physical characteristics of the point sources and diffuse emission across the region. In general, the point source spectra are all associated with sites of active star formation. By contrast, the extended emission spectra trace the HII and PDR emission that is photoexcited by the massive stellar population dispersed across the region. For this dataset, we find two distinguishing features in the ionic line emission that are specially worth noting.

(1) [SIV] 10.51 μm emission is largely undetected among the point source spectra but is detected in all of the extended emission spectra.

(2) [NeII] 12.81 μm is detected in every point source and extended emission spectrum with only two exceptions among the point source spectra.

The strong [SIV] line, due to ionization of the interstellar gas by the O star population, is seen in the extended emission spectra across the region (see Figures 17 and 18). [SIV] and [NeII] are often found in sites of active star formation, e.g. giant HII regions (Lebouteiller et al. 2008), blue compact dwarf galaxies (BCDs; Wu et al. 2006), and starburst galaxies (Brandl et al. 2006; Bernard-Salas et al. 2009a). Our analysis differs from previous works by separating the diffuse emission from the infrared point source emission. We show that the dense regions embedded in the PDR do not generally show [SIV] emission. The absence of [SIV] in most of the point source sample is likely because the heating sources at the point source locations are not hard enough to triply-ionize sulfur. The gas density at these positions can be estimated from the [SIII] 18.71 μm and 33.48 μm

lines fluxes from high-resolution *Spitzer* data at the point source positions published in Lebouteiller et al. (2008). The ratio of these two lines ranges from 0.43-2.7, suggesting densities of $n_e T_4^{1/2} < 3 \times 10^3$ cm^{-3} for the lowest value ratio and below about 10^2 cm^{-3} for most of the positions, well less than the critical densities of n_{crit}([SIV])= 5.4$\times$ 10^4 cm^{-3} n_{crit}([NeII])= 6.5$\times$ 10^5 cm^{-3}. It should be noted that these estimates for the [SIII]-derived gas density are subject to the diffuse as well as the dense material at these positions because the point source emission cannot be treated separately from the diffuse emission in the high-resolution modules as it can for the low-resolution modules.

4.3. PAH Feature Profiles

In order to classify the PAH spectra observed in N66, we plot example high signal-to-noise (S/N) N66 PAH spectra versus templates in the 7-9 μm range and 11-12 μm range from Peeters et al. (2002) and van Diedenhoven et al. (2004) respectively in Figures 8 and 10. Peeters et al. was able to classify the 6-9 μm PAH features based on their peak centroids, and discovered that there is a relationship with environment: Class A spectra are typical for HII regions and non-isolated Herbig AeBe stars, Class B spectra are more typical for isolated Herbig AeBe stars, and Class C spectra are more common in evolved stellar systems. van Diedenhoven et al. studied the 11.3 μm PAH complex and developed templates for Classes A and B only.

The N66 spectra for the 7.7 μm and 8.6 μm features (Figure 8) are generally most similar to the Class A template, as is expected for an HII region. However, in some of the spectra, the 7.7 μm features appear to be wider than the templates. For the 11.3 μm PAHs, the observed line centers appear to be slightly redshifted with respect to the Orion Nebula (Figure 9); i.e. less than one resolution element. However, this is the only feature in the N66 spectra, ionic, molecular, or PAH, which shows a centroid shift, and while such

a systematic offset could very well be due to continuum subtraction it is deserving of closer attention.

Therefore, the available high-resolution spectra (R $\sim$ 600) of N66 were reduced for comparison with the PAH templates from van Diedenhoven et al. (2004) (Figure 10). Labelling for these spectra, first used in Lebouteiller et al. (2008), follows that work. Unfortunately, the SH data have a low S/N. However, in the spectra for positions 1, 2, 3, and 5, a narrow line, 2-3 wavelength elements wide, that corresponds to the position of the HI 9-7 11.31 μm line, is visible. Due to the fact that the raw images do not reveal single pixels with high values at this wavelength, it is not likely that this line is due to improperly calibrated pixels on the array, but is an actual astronomical feature. In order to determine whether the narrow line at 11.3 μm is the HI 9-7 line, we compared the line strength to that of the detected HI 7-6 12.37 μm line to see if their ratio is consistent with case B recombination theory (Hummer & Storey 1987). We used a temperature of 12,500 K and a number density of 10^2 cm^{-3} to compare to the data; N66 has measured values of 12,269 K average and 50-500 cm^{-3} (Oliveira et al. 2008; Tsamis et al. 2003; Peimbert et al. 2000; Dufour & Harlow 1977). For case B,

$$\frac{HI\ 9-7}{HI\ 7-6} = 0.223 \tag{1}$$

For sources 1, 2, and 3, the ratio was about 0.2, and for source 5, it was < 0.1. Considering the low S/N of these data, but also considering the other detected HI lines (HI 7-6 line in hi-res and the HI 6-5 line at lo-res), it is likely that the detected line is the HI 9-7 line and that this line is contributing to the apparent redshift of the 11.3 μm feature.

Leaving aside the narrow line, there are still several cases in which the peak of 11.3 μm PAHs in N66 are slightly redward ($\Delta\lambda \sim 0.1$ μm) of the two templates (positions *8, 9, 10* and *13* show it most clearly in spite of the low S/N). According to the *Spitzer* IRS

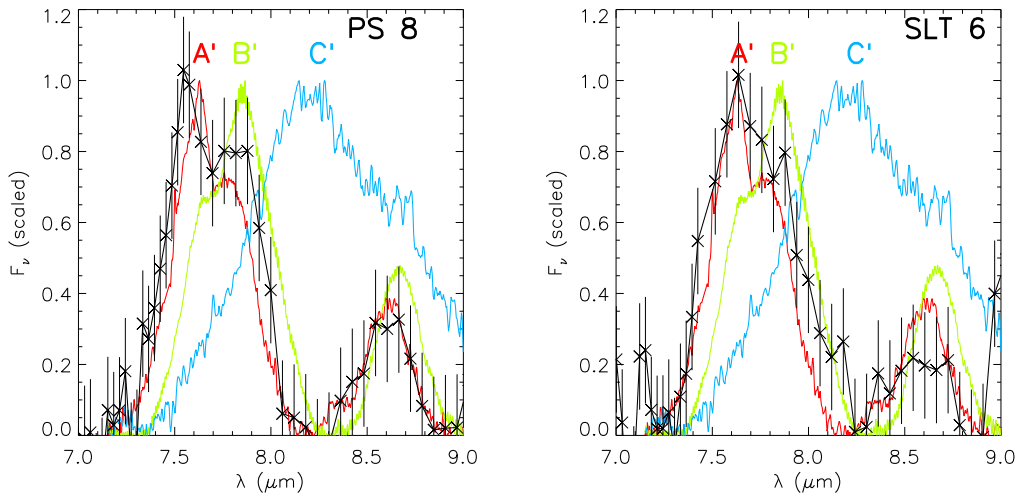

Fig. 8.— Example 7.7 μm and 8.6 μm PAH features are plotted versus the Peeters et al. (2002) templates (templates are from ISO SWS, with R $\sim$ 450 for classes A and C and $\sim$ 1500 for class B), showing both the width of the 7.7 μm feature and the suppressed 8.6 μm emission in the right panel. For the spectra of the extended emission, the strong lines at 7.46 μm and 8.99 μm are HI 6-5 and [ArIII] respectively. The N66 spectra by and large resemble the class A template, as expected for a giant HII region. Spectra were scaled so that the peak of the 7.7 μm feature matched that of the templates.

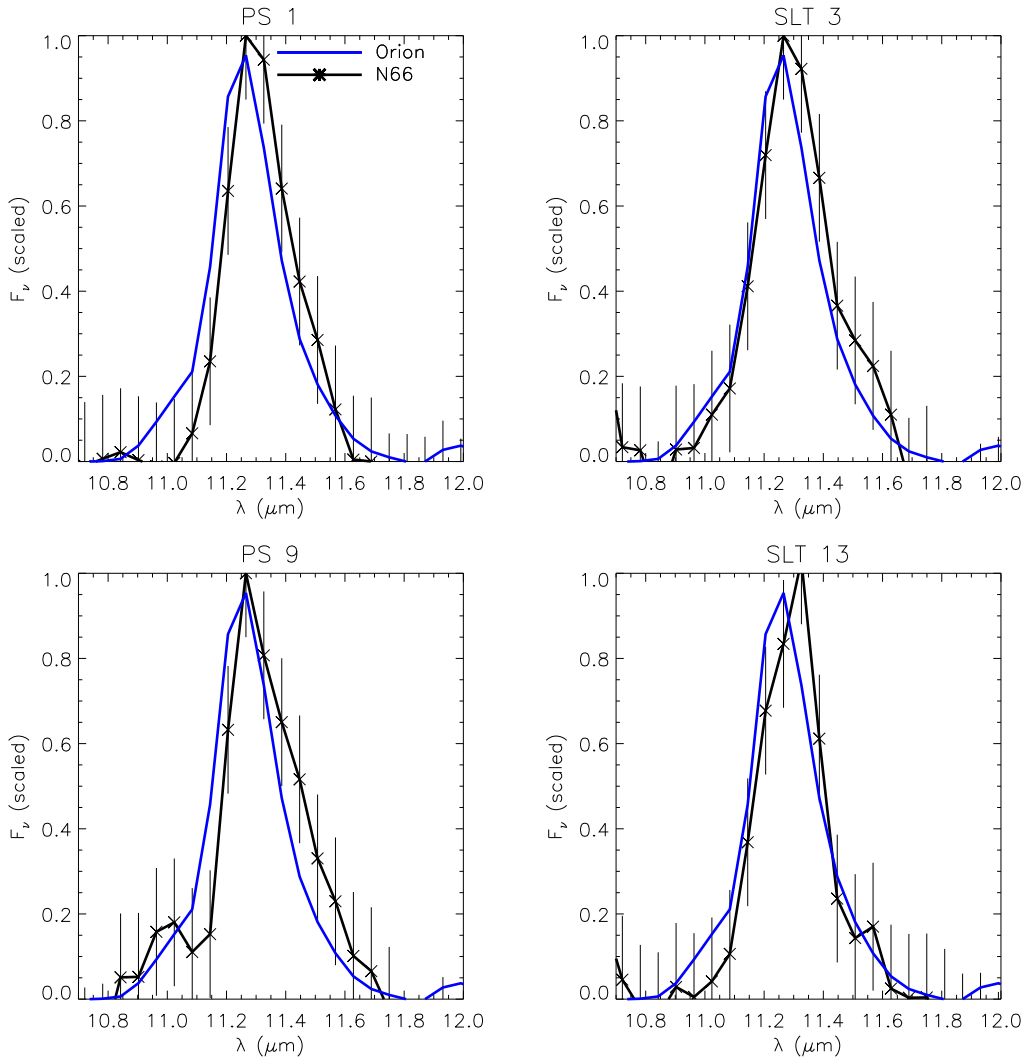

Fig. 9.— Example 11.3 μm PAH spectra in black are plotted against a SL spectrum of the Orion nebula. The N66 spectra appear to have peaks that are redward of the Orion spectra.

instrument handbook[3] the wavelength calibration is good to 1/5 of a resolution element, or, for SH, ~ 0.001 μm. Pointing offsets are also a minor concern, but could produce a 0.5-pixel shift, or ~ 0.04 μm. Both of these potential errors are small in comparison to the ~ 0.1 μm shift in the PAH feature centroid, would additionally affect all features in this spectral order, and therefore cannot account for the shift seen. We must stress once again that continuum subtraction may play a role in the centroid mismatch. If born out, this is the only ISM-type environment observed so far that exhibits a profile redshifted compared to class A. We also note the absence of the 11.0 μm feature seen in the templates, though its absence is likely due to the low S/N of these spectra.

While the observed wavelength shifts across N66 appear in both point source and ISM spectra, a worthwhile comparison is Herbig AeBe stars, which often exhibit 11.3 μmPAH peaks that are shifted redward by a similar amount. (Sloan et al. 2005; Keller et al. 2008) show peak shifts in both the 7.7 μm and 11.3 μm PAH complexes. It is interesting that we do not see an appreciable shift in the 7.7 μm feature, which is often shifted by as much as 0.3 μm or more in Herbig AeBe environments and would therefore be detectable with our spectra.

Because the redward shift of the 11.3 μm PAH complex is small (0.1 μm) and the detected HI 9-7 line must be resolved out of the feature, we recommend that high-resolution and high S/N follow-up observations be made. JWST's MIRI instrument, with its spectral resolution of ~ 3000, is a perfect candidate instrument for such follow-up. Such observations would be capable of not only confirming the wavelength shift of the PAH and more accurately determining the line flux and width of the narrow line, but, an expanded high-resolution study could be used to determine whether these features are peculiar to N66

[3]The IRS instrument handbook may be found online at: http://irsa.ipac.caltech.edu/data/SPITZER/docs/irs/irsinstrumenthandbook/

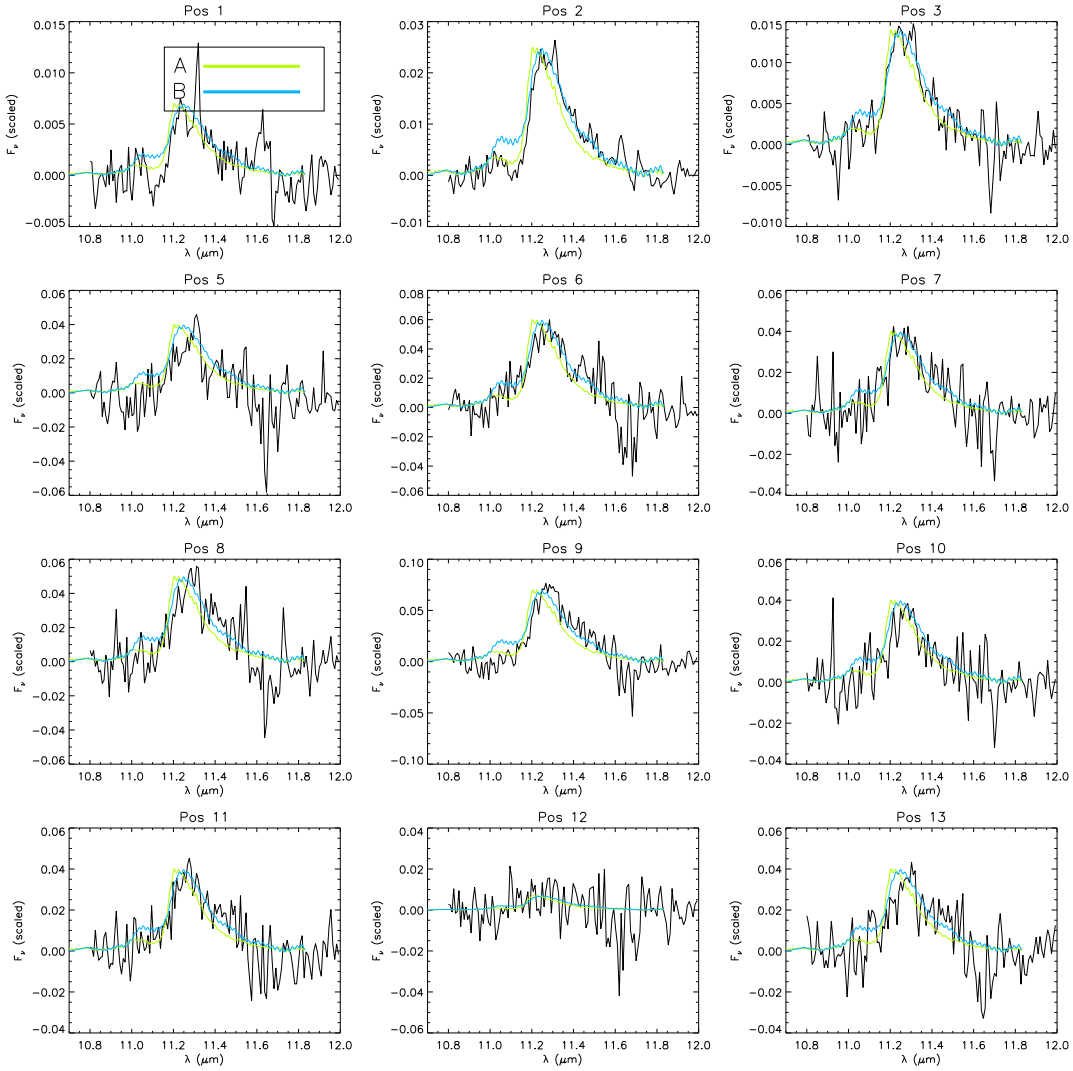

Fig. 10.— The 11.3 μm PAH for all of the *IRS* SH pointings are plotted versus class A and class B PAH template spectra from van Diedenhoven et al. (2004). The N66 spectra are scaled to best fit the templates, excluding the possible HI 9-7. For several sources, there are prominent shifts that are independent of the HI line (most notably position 8, 9, 10, and 13).

(or, perhaps, the SMC), or are systematic at low metallicity.

4.4. 14 μm Continuum Emission

The continuum between 13.5 and 14.2 μm is due to emission by a combination of very small carbonaceous dust grains (VSGs: a $>$ 50 Å; Li & Draine 2001) and warm large dust grains. However, we expect the VSGs to dominate the emission at these wavelengths; Draine & Li (2007), § 5, notes that the VSG contribution to the continuum at $\lambda < 20$ μm is roughly independent of the radiation field strength because it results from single-photon heating.

The 14 μm continuum is measured as the continuum beneath the PAH bands as fit with PAHFIT. Figure 11 plots the 14 μm continuum over [SIV] versus the radiation field hardness as traced by [SIV]/[NeII] for the extended emission spectra. By normalizing the 14 μm continuum emission by the [SIV] line flux, we are able to compare the dust continuum emission to the radiation field strength, and then plot that value versus the radiation field hardness. There is an anti-correlation that suggests that the 14 μm continuum is weakest where the radiation field is hardest and strongest. Weaker continua in harder and stronger radiation fields supports the assertion first presented in Contursi et al. (2000) that the VSGs are likely being photodestroyed by the U = 10^5 ISRF radiation field in N66.

Because the correlation seen in Figure 11 is roughly linear excluding the outlier, this supports the assertion that the 14 μm emission is mostly due to VSGs, not large grains; if there was a substantial contribution from large grains to the 14 μm continuum, then the expected variations in large grain dust temperature across the region would make this trend non-linear.

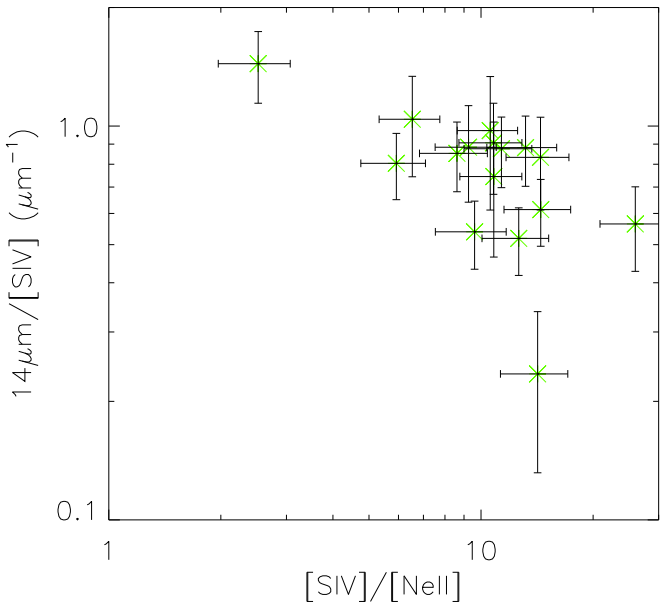

Fig. 11.— The 14 μm continuum divided by [Siv] flux in the extended emission versus [Siv]/[Neii]. These data show an anti-correlation that suggests that the 14 μm continuum is weakest in the hardest and strongest radiation fields.

4.5. PAH Ratios as Diagnostics

There are four major PAH features in the 5-15 μm wavelength range. These features are identified by specific resonant modes inside the PAHs (Allamandola et al. 1989; Draine & Li 2007). (1) The 6.2 μm feature is created by an aromatic C-C stretch mode. (2) The 7.7 μm feature is also due to C-C aromatic stretch modes. (3) The 8.6 μm feature is emitted by a C-H in-plane bending mode, while (4) the 11.3 μm feature is due to a solo C-H out-of-plane bending mode and is sensitive to edge structure (Hony et al. 2001; Allamandola et al. 1989; Puget & Léger 1989). Furthermore, the 6.2, 7.7, and 8.6 μm PAH features are attributed to ionized PAHs, whereas the 11.3 μm PAH feature is attributed to neutral PAHs (Hudgins & Allamandola 1999), and there is believed to be a wavelength-size dependence for PAHs, wherein larger PAHs emit most efficiently in the longer-wavelength PAH features (Draine & Li 2007; Schutte et al. 1993).

PAH ratios offer an independent assessment of the ISM's physical characteristics. Galliano et al. (2008b) found an average correlation between the $I_{7.7}/I_{11.3}$ and $I_{6.2}/I_{11.3}$ for a sample of starbursts, BCDs, HII regions and PDRs, reproduced in Figure 12, where Galliano's average is shown as a solid line with the one-σ standard deviation plotted on either side of the average. The data points for N66 are also plotted, with the point source data as red triangles and the extended emission data as green stars. The point source data show a range of $I_{7.7}/I_{11.3}$ from $\sim$ 0.03-6.3, over two orders of magnitude, in a relatively narrow range of $I_{6.2}/I_{11.3} \sim$ 0.5-1.8. The extended emission spectra have respective ranges of 0.35-8.4 and $\sim$ 1-3. Averaging together all values for the $I_{6.2}/I_{11.3}$ and $I_{7.7}/I_{11.3}$ ratios weighted by feature strength, the point sources have values of 1.1 and 2.7 and the extended emission have values of 1.4 and 3.7 respectively. These averages are relatively close together and lie within the galaxy sample's average correlation.

However, the wide spread around those averages suggests an intriguing variety of

physical attributes. For instance, the massive embedded YSO (PS7, discussed in detail in Section 4.1.3) has a very high $I_{7.7}/I_{11.3}$ ratio value; see Figure 12. This might suggest that the PAH emission from the embedding envelope is either more heavily ionized than other point sources, or else the average PAH size is smaller. Having a population of ionized PAHs in the YSO environment seems unlikely because the temperature of a Class I YSO is probably very low (∼250 K; Myers et al. 1998). The HII regions N66B and N66C (PS5 & PS6) both lie near the average value for $I_{7.7}/I_{11.3}$, but NGC 346 (PS9) lies well off of this average, with an outlying value of ~ 0.03. The low value for the 7.7 μm feature strength in NGC 346 is confirmed with a visual inspection of the spectrum - see the Appendix, Figure 16. As an opposite example to the YSO, NGC 346 may either contain a largely neutral PAH population or else very large PAHs; the latter solution seems most sensible given the numerous blue stars in the cluster.

The lack of correlation seen in Figure 12 is intriguing because the 6.2 μm and 7.7 μm PAH features are generally very tightly correlated for spectra of HII regions and entire galaxies (Vermeij et al. 2002; Galliano et al. 2008b), for planetary nebulae (Bernard-Salas et al. 2009b), and in the reflection nebula NGC 2023 (Peeters et al. 2013 in preparation). We have already determined that this is not due to the decomposition method (see § 3.3). The same lack of trend can be seen with the column-extracted PAH fluxes from Lebouteiller et al. (2011), although a weak correlation may be seen in the Sandstrom et al. (2012) results for the high S/N data points. We are not aware of any other mention in the literature of a decoupling of the 6.2 μm and 7.7 μm PAH features in this manner.

To study general trends, the $I_{7.7}/I_{6.2}$ and $I_{8.6}/I_{6.2}$ are plotted against $I_{7.7}/I_{11.3}$ in Figure 13. A trend is seen in the $I_{7.7}/I_{6.2}$ versus $I_{7.7}/I_{11.3}$ ratios plot that was not recorded in the Galliano et al. dataset. The values of the $I_{7.7}/I_{11.3}$ ratio seem to suggest that the areas of extended emission (on the right) are largely photoionized whereas the point sources

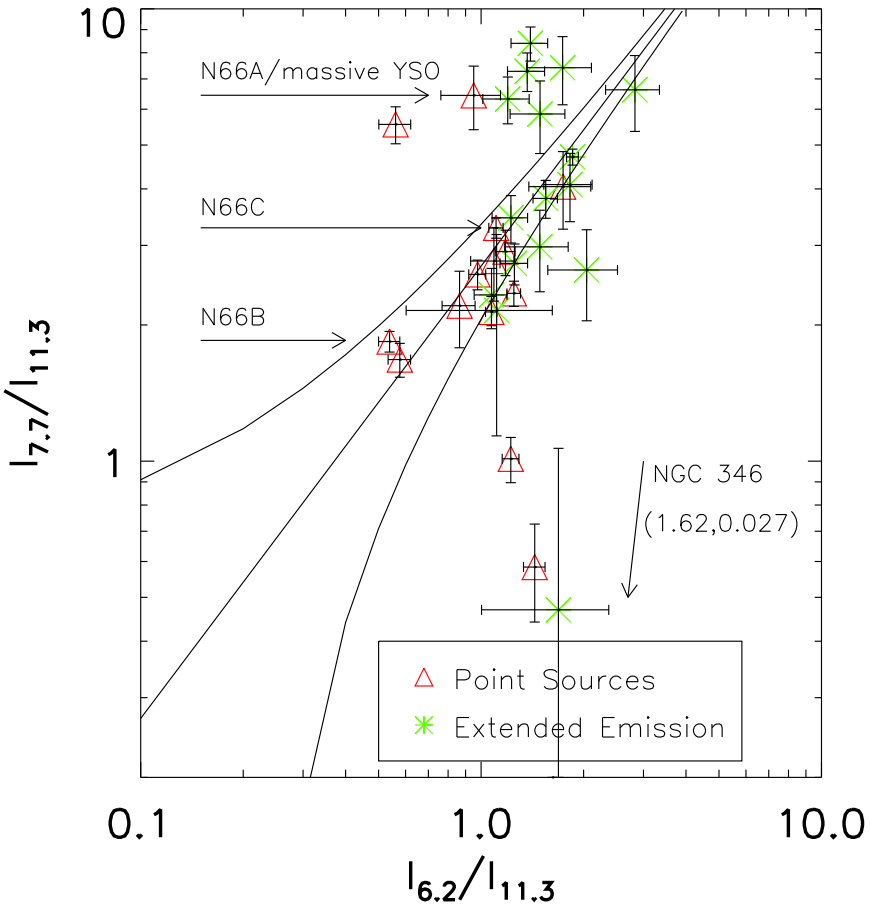

Fig. 12.— The average $I_{7.7}/I_{11.3}$ versus $I_{6.2}/I_{11.3}$ from Galliano et al. (2008b) Figure 3 is plotted as the solid line with its 1-σ spread shown. The N66 data points are overplotted.

(on the left) are more neutral, with some exceptions. The variation of the $I_{7.7}/I_{6.2}$ ratio might suggest some photoprocessing effect: the 6.2 μm PAH flux becomes weaker in harder radiation fields due to the destruction of the smaller PAH molecules.

There is no trend between the $I_{8.6}/I_{6.2}$ and $I_{7.7}/I_{11.3}$ PAH ratios. Because the $I_{8.6}/I_{6.2}$ ratio should be independent of ionization state and therefore should trace the size of the PAHs, while the $I_{7.7}/I_{11.3}$ ratio does trace ionization state, it appears that the size distribution is *independent of ionization state*. This includes both point sources and extended emission spectra, and it should be noted that a spread of about one order of magnitude still exists in the $I_{8.6}/I_{6.2}$ ratio values. We therefore conclude that N66 shows no evidence of local variation in the N_C^{min} value due to the ionization state for the PAH population, but it is unclear how this result should compare to galaxies with significantly different metallicity or star formation activity.

In Sandstrom et al. (2012), the weak 7.7 μm feature across the entire SMC, including N66, and the relatively strong 11.3 μm feature suggested to the authors that PAHs across the SMC are both small and mostly neutral. However, the authors used a stringent signal-to-noise cut-off, thereby excluding extended emission from their analysis and biasing their results towards the conditions found for our point source spectra. When our data are compared against the grey data points in the PAH ratios plots in Sandstrom et al. (2012), it is interesting to note that the results from the map agree well with our targeted spectroscopy results. What our analysis is able to show is that the point sources lie in a similar PAH ratio space to the extended emission, despite the different physical conditions as discussed. Furthermore, it is clear that the PAH population exists on a spectrum, from more neutral in the dense PDR where the point sources lie, to more ionized in the diffuse PDR and HII region.

The PAH population size distribution in low-metallicity environments is a contentious

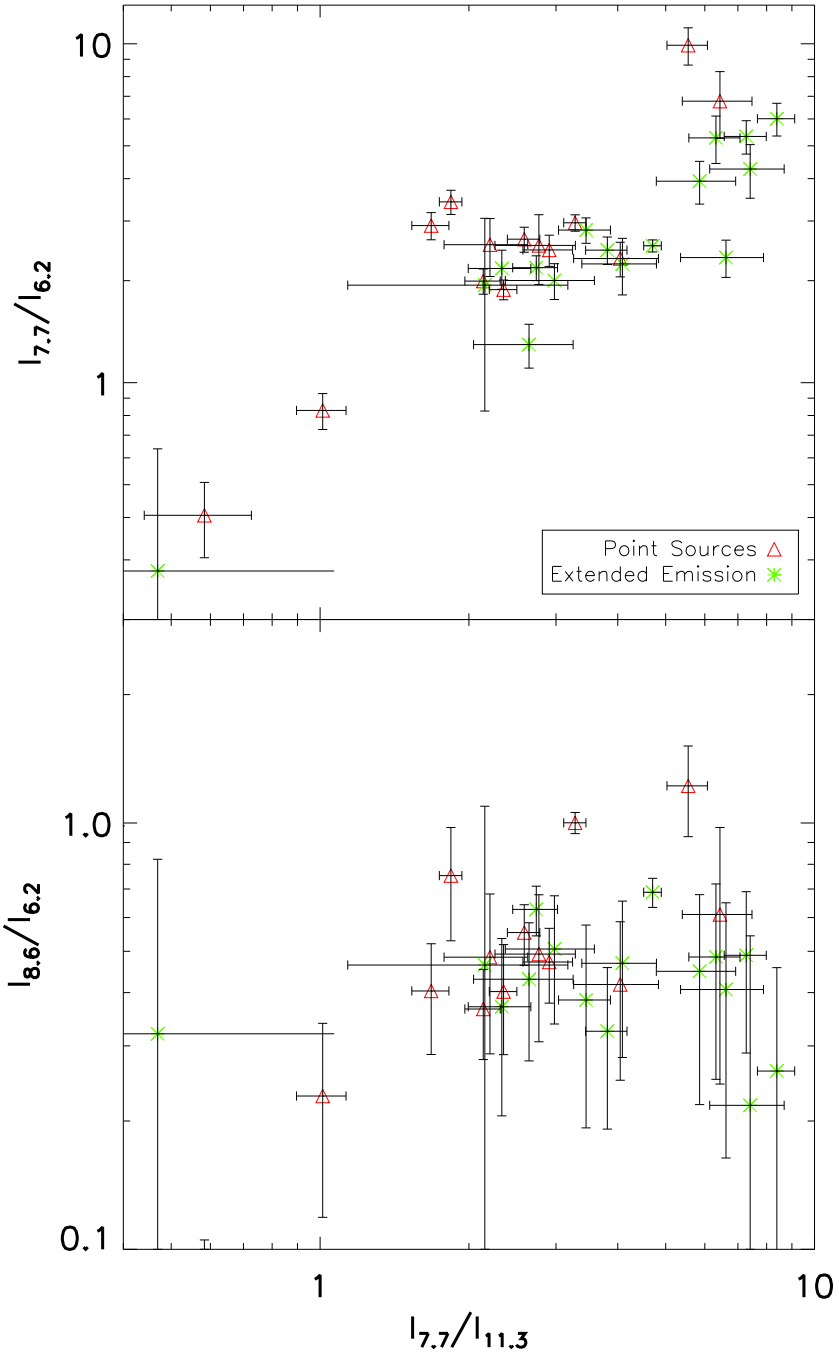

Fig. 13.— The $I_{7.7}/I_{6.2}$ and $I_{8.6}/I_{6.2}$ versus $I_{7.7}/I_{11.3}$ PAH ratios are plotted for N66.

topic. In a study of low-metallicity BCDs, Hunt et al. (2010) found relatively strong $I_{8.6}$ and $I_{11.3}$ features and interpreted this finding to mean a large N_C^{min} value for PAHs. The analysis of the $I_{17}/I_{11.3}$ PAH ratio by Smith et al. (2007) suggests the opposite, that low-metallicity environments (12+log(O/H) $\lesssim$ 8.1) host PAH populations with small sizes on average. We do not have the long-wavelength data to sufficient depth or spatial resolution for a $I_{17}/I_{11.3}$ analysis; however, that data is available in the Sandstrom et al. (2012) maps, and they determine that the N_C^{min} value is smaller in the SMC than in the Milky Way based on the weak 17.0 μm PAH feature. Our own results, including a wide range of $I_{8.6}/I_{6.2}$ ratio values, suggest that these average trends do not hold on small size scales, where local effects likely come in to play.

4.6. N66 PAH Emission in Context

In this section, we compare the PAH and forbidden line emission for N66 with data from other sources with similar star formation environments to N66, including giant HII regions and blue compact dwarf galaxies (BCDs). For the PAH emission, we take the ratio of the 11.3 μm and 6.2 μm PAH features which will trace the ionization state of the PAHs and also the PAH size distribution. For the gas, we take the [SIV]/[NeII] ratio as a tracer of the radiation field hardness. The other giant HII regions studied are 30 Doradus and NGC 3603 (Lebouteiller et al. 2008, 2011), and the population of well-studied BCDs comes from Wu et al. (2006). The results are plotted in Figure 14.

The N66 point sources have PAH ratio values similar to sources with small [SIV]/[NeII] ratio values. However, the extended emission spectra, whose [SIV]/[NeII] ratio is on average higher than most other sources, also exhibits a lower $I_{11.3\mu m}/I_{6.2\mu m}$ value, as was discussed in § 4.5, suggesting that the PAH population in the diffuse ISM of N66 is more ionized than in the other HII regions and in integrated spectra of BCDs, despite sometimes equally hard

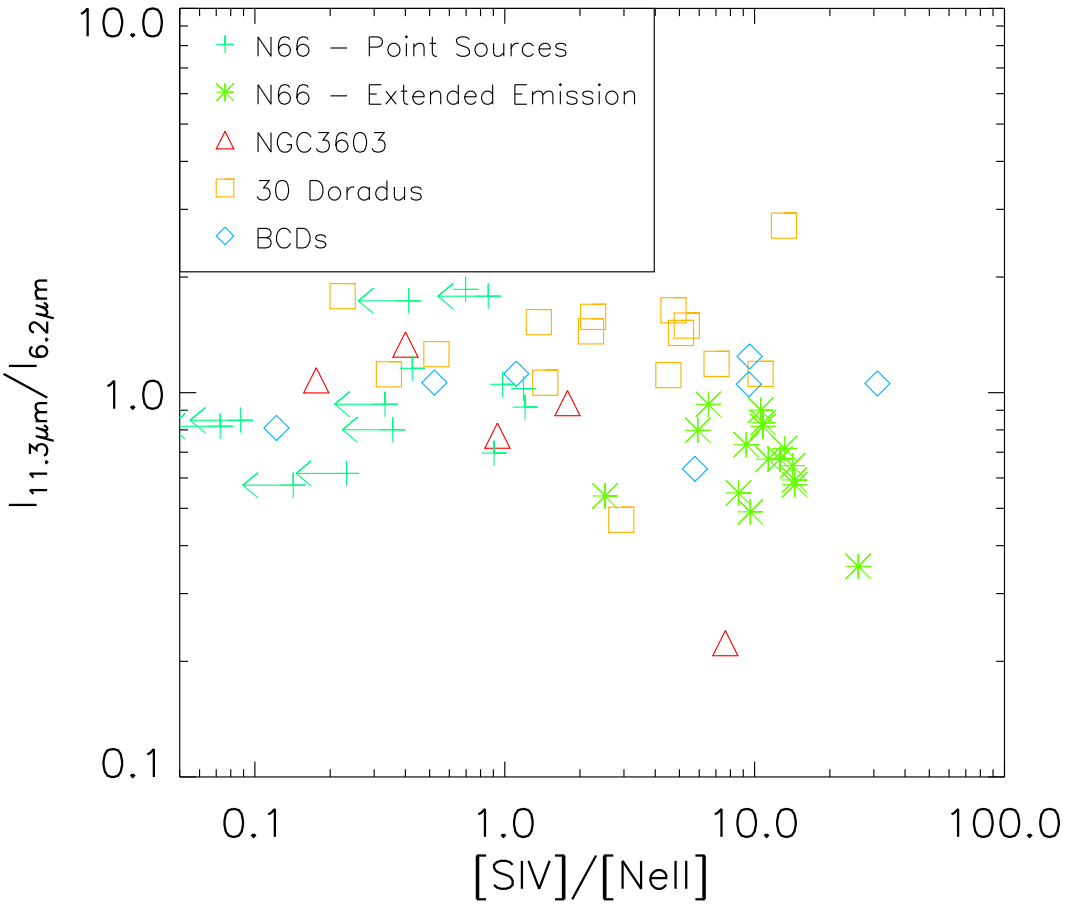

Fig. 14.— The PAH ratio $I_{11.3}/I_{6.2}$ versus [SIV/[NeII] for N66 point sources (plus signs) and extended emission spectra (stars) plotted along with results for NGC 3603 (triangles), 30 Doradus (squares), and some well-studied BCDs (diamonds). References for these data are given in the text.

ISRFs as traced by the [SIV]/[NeII] ratio.

There is a source of bias in this comparison worth noting. The spectra of 30 Doradus, NGC 3603, and the BCD sample were not extracted using SMART-AdOpt as described in § 3.2. Instead, they are all composite spectra. For the giant HII regions NGC 3603 and 30 Doradus, each spectrum likely has contributions from both unresolved point sources in the PDR and diffuse HII emission. For the BCDs, each spectrum likely contains emission from both star-forming and quiescent regions. It is therefore not surprising that the results for N66 are both separated and qualitatively different from those of the other regions.

4.7. Fraction of PAH Emission Coming From the Point Sources

The SMC (including N66) is the closest low-metallicity star forming galaxy to the Milky Way and can therefore be used to study possible trends to other low-metallicity star-forming environments. It is therefore important to determine what the dominant source of the PAH emission in N66 is, in order to properly interpret unresolved HII region studies. Does the PAH emission primarily come from the high S/N point sources, or from the diffuse ISM in the HII region and PDR?

Using the spectral maps of N66 presented in Sandstrom et al. (2010, 2012) in order to study a spatially well-sampled dataset, we made maps of the 6.2 μm and 11.3 μm PAH features by subtracting away the continuum measured locally. The 7.7 μm feature straddles the SL1 and SL2 orders and the 8.6 μm feature is very hard to pick out from the continuum, so these two features were excluded from the analysis. The average brightness in the PDR was measured and then point sources were defined as anything that was 3-σ above the average; the annulus selected around each point source was 6 pixels across, or 10.8 $''$. Using this metric, we summed up the emission for point sources as well as the

diffuse emission from the entire map in the 6.2 μm and 11.3 μm PAH features. There are a total of 13 selected point sources in the 6.2 μm map, and 14 in the 11.3 μm map, and the map is $300'' \times 430''$. We find that the fraction of the PAH emission coming from the point sources is $28 \pm 8\%$ for the 6.2 μm PAH feature and $21 \pm 6\%$ for the 11.3 μm PAH feature. Due to the relatively high level of variance between these two PAH features, we conclude that, as a rough proxy for studies of unresolved star formation at low-metallicity, the point sources (resolved down to $\sim$ 2 pc) contribute roughly $\sim$ 20-35% of the PAH emission across the region. This means that it is the extended emission which dominates the observed PAH brightness in N66, and possibly low-metallicity giant HII regions generally.

5. CONCLUSION

N66 is the largest starburst in the SMC and contains half of the entire galaxy's O stars. Its hard radiation field and low metallicity make it an excellent corollary to studies of BCDs and high-redshift starbursts. Our analysis of *Spitzer/IRS* spectra from 5-14 μm makes use of powerful optimal extraction routines that separate emission from the dense PDR's unresolved point sources and the surrounding ISM's more diffuse emission. The point sources are all associated with sites of active star formation in the region. Of special note are the spectroscopic confirmation of a massive embedded class I YSO, the detection of silicates associated with young ($\sim$ 3 Myr) stellar clusters, and the detection of PAHs and silicates associated with a B[e] star that indicates it may in fact be a Herbig AeBe star. In the diffuse ISM, we find evidence that the very small grains are being photodestroyed, consistent with previous studies of N66. The PAH emission shows several interesting features. The 11.3 μm PAH complex has an unexplained centroid shift for both point sources and the diffuse ISM. In general, the PAHs are best classified as type A. However, a slight widening of the 7.7 μm feature in some of the spectra is either due to the 7.46 μmHI

6-5 line in the diffuse emission spectra, or else the removal of ISM contamination that reveals type B-like circumstellar features. The 6.2 μm and 7.7 μm PAH band fluxes in N66 do not correlate with each other, an observation that we do not believe has been observed in other objects. Because we were able to separate out the point source and extended emission in the spectral slit, the conclusions we draw from the PAH ratios are detailed where those presented in Sandstrom et al. (2012) are more general: we find that the PAHs are more neutral in the densest parts of the PDR (including the entire point source catalogue), and more ionized in the diffuse ISM while Sandstrom et al. determined that the PAHs were on average more neutral than in higher-metallicity galaxies. On average, Sandstrom et al. found that PAHs in the SMC are smaller compared to those in more metal rich galaxies. We show that on small scales, the size distribution of the PAHs in N66 (based on the 8.6 μm PAH feature flux) does not appear to be correlated with their ionization state and is therefore independent of the ratio of UV field strength to electron density. We stress that, on average, our results match the work of Sandstrom et al. (2012) extremely well, and that the spread in ionization state and lack of clear trend with minimum PAH size on small scales is made possible by our spectral extraction techniques. Lastly, we have determined using spectral maps of the region that only $\sim$ 20-35 % of the PAH emission in N66 is coming from the unresolved point sources, and it is therefore dominated by the diffuse emission. This percentage suggests that studies of unresolved low-metallicity star-forming regions in nearby BCDs and starburst galaxies will also have PAH spectra dominated by the diffuse HII region and PDR, not the unresolved point sources, and the observed PAH signatures of the point source spectra are therefore not representative of the entire HII region's properties.

The authors would like to thank the anonymous referee, whose comments helped to improve the manuscript. DGW would like to thank K. Sandstrom for discussions concerning

the PAH spectra of N66, E. Muller for discussions about the molecular gas content, and P. Martini and A. Leroy for helpful suggestions. KEJ gratefully acknowledges support for this paper provided by NSF through CAREER award 0548103 and the David And Lucile Packard Foundation through a Packard Fellowship. JSB wishes to acknowledge the support from a Marie Curie Intra-European Fellowship within the 7th European Community Framework Program under project number 272820.

A. The Atlas of Reduced Spectra

The spectra used in the analysis are presented here. The reduction method for producing the point source and extended emission is discussed in § 3.2.

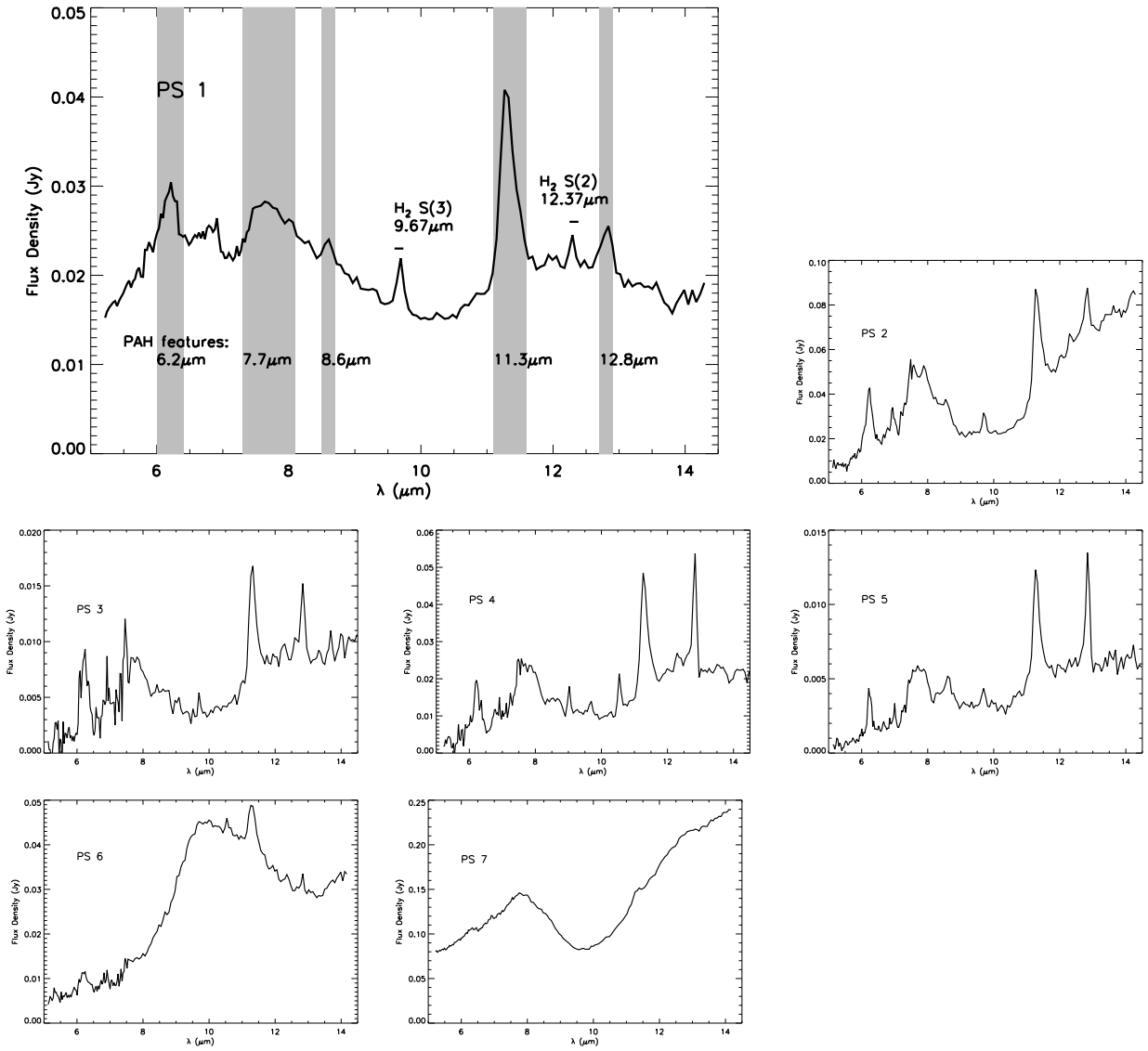

Fig. 15.— *Spitzer* spectra of point sources PS1-PS7. The spectrum of PS1 is enlarged so that the PAH and H_2 feature labels can be seen clearly.

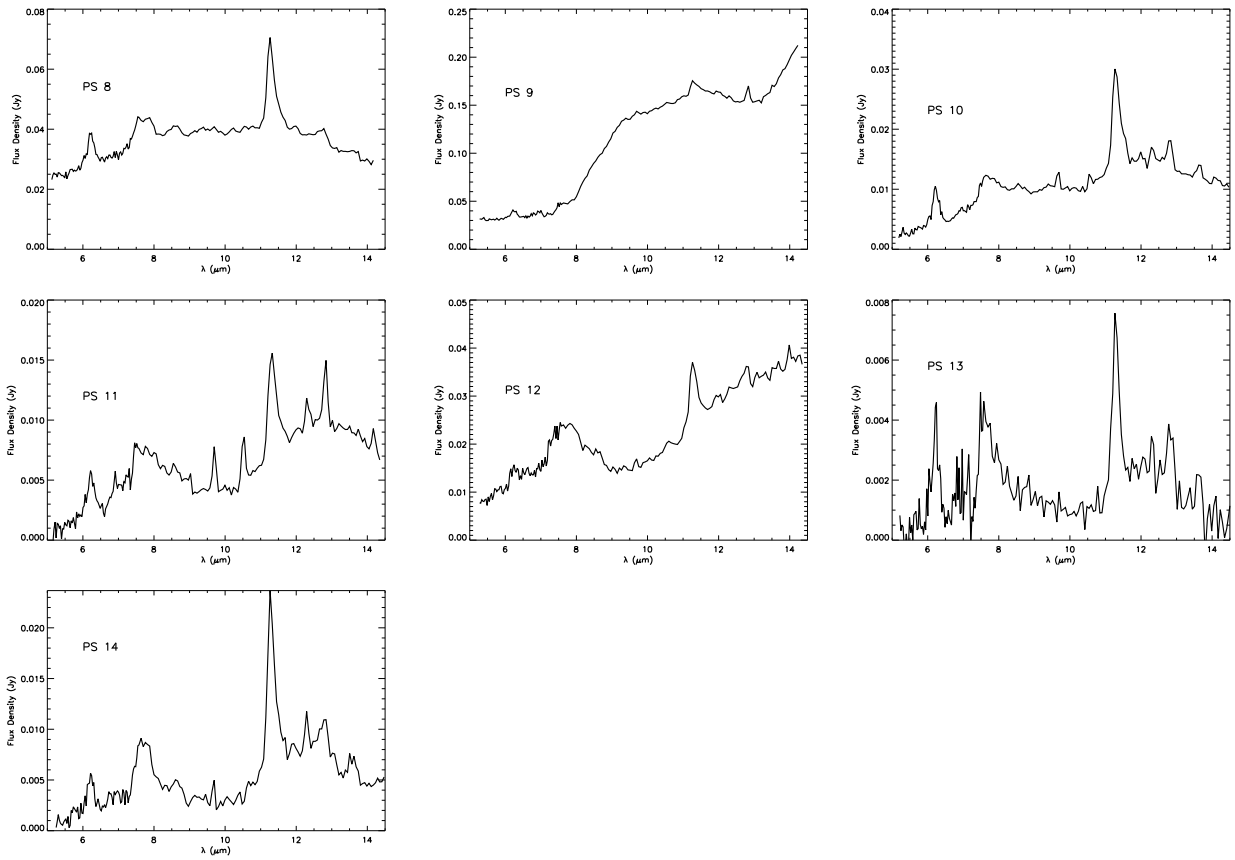

Fig. 16.— *Spitzer* spectra of point Sources PS8-PS14.

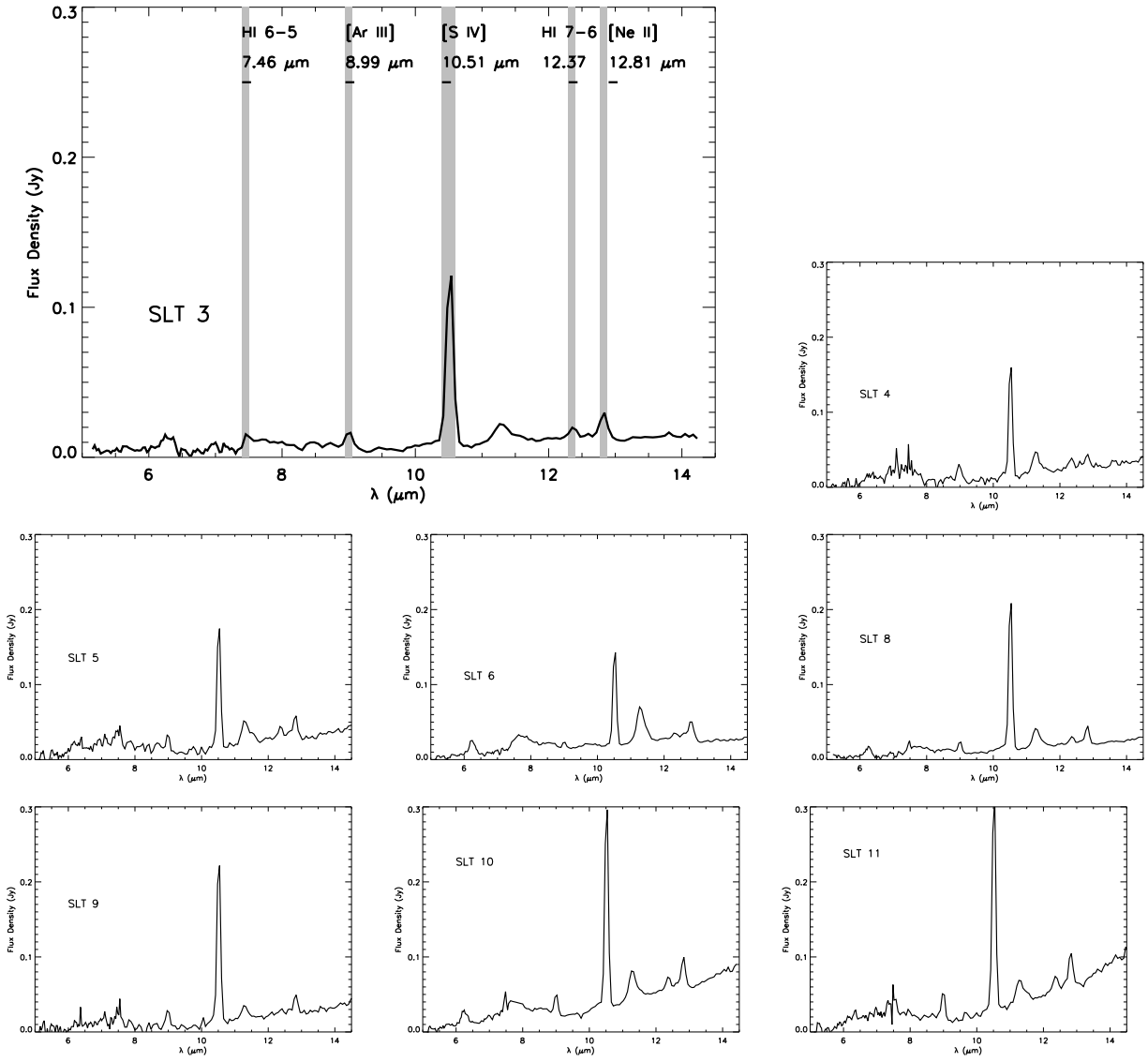

Fig. 17.— *Spitzer* extended emission spectra SLT3-SLT11. The spectra are all plotted on the same scale, so that the relative flux in each slit can be seen. The spectrum for SLT3 has been enlarged so that the atomic and ionic line labels can be see clearly.

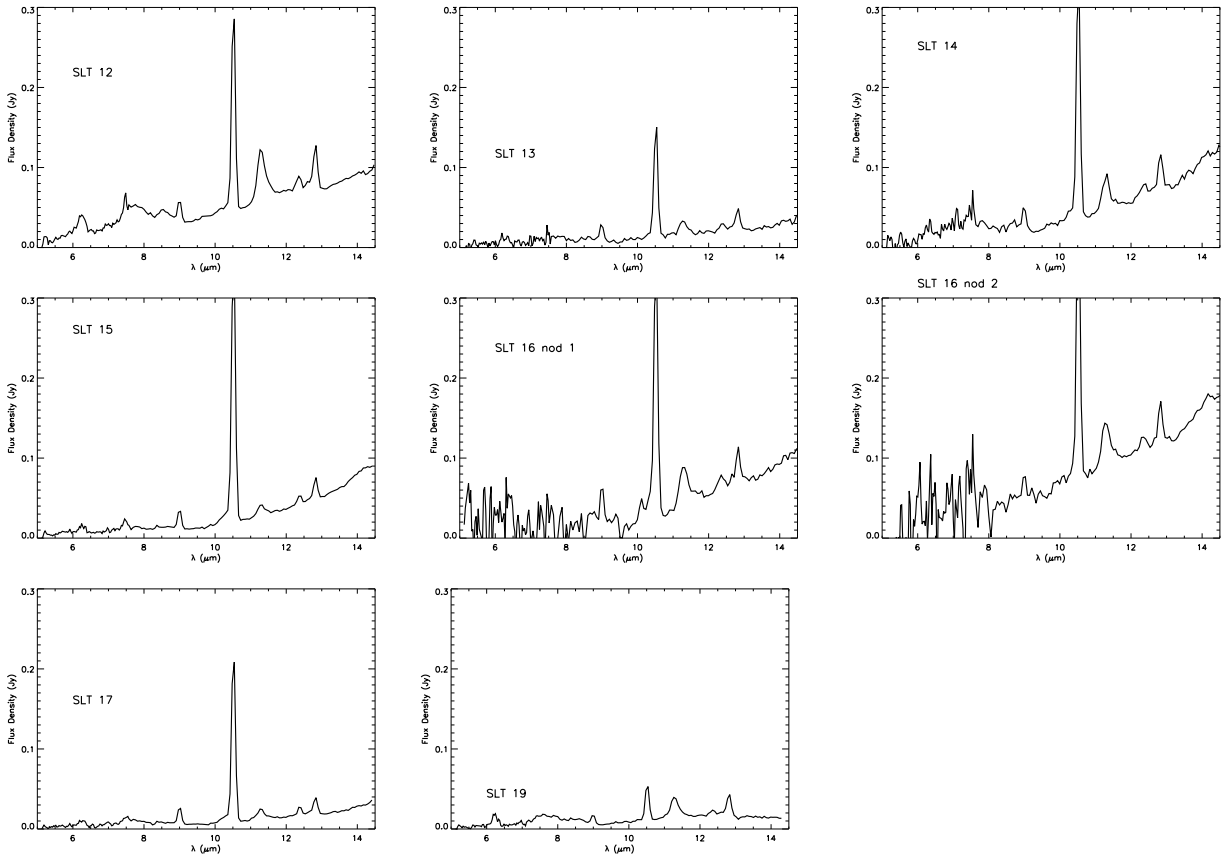

Fig. 18.— *Spitzer* extended emission spectra SL12-SLT19. The spectra are all plotted on the same scale, so that the relative flux in each slit can be seen.

REFERENCES

Allamandola, L. J., Tielens, A. G. G. M., & Barker, J. R. 1989, ApJS, 71, 733.

Bakes, E. L. O., & Tielens, A. G. G. M. 1994, ApJ, 427, 822.

Bernard-Salas, J., Spoon, H. W. W., Charmandaris, V., et al. 2009, ApJS, 184, 230.

Bernard-Salas, J., Peeters, E., Sloan, G. C., et al. 2009, ApJ, 699, 1541.

Bouret, J.-C., Lanz, T., Hillier, et al. 2003, ApJ, 595, 1182.

Brandl, B. R., Bernard-Salas, J., Spoon, H. W. W., et al. 2006, ApJ, 653, 1129.

Caplan, J., Ye, T., Deharveng, L., Turtle, A. J., & Kennicutt, R. C. 1996, A&A, 307, 403.

Compiègne, M., Abergel, A., Verstraete, L., et al. 2007, A&A, 471, 205.

Contursi, A., Lequeux, J., Cesarsky, D., et al. 2000, A&A, 362, 310.

Cox, N. J. L., Cordiner, M. A., Ehrenfreund, P., et al. 2007, A&A, 470, 941.

can Diedenhoven, B., Peeters, E., Van Kerckhoven, C., et al. 2004, ApJ, 611, 928.

Draine, B. T., & Li, A. 2007, ApJ, 657, 810.

Dufour, R. J., & Harlow, W. V. 1977, ApJ, 216, 706.

Fazio, G. G., et al. 2004, ApJS, 154, 10.

Furlan, E., Luhman, K. L., Espaillat, C., et al., & Fischer, W. J. 2011, ApJS, 195, 3.

Galliano, F., Madden, S. C., Tielens, A. G. G. M., Peeters, E., & Jones, A. P. 2008, ApJ, 679, 310.

Gouliermis, D. A., Dolphin, A. E., Bradner, W., & Henning, T. 2006, ApJS, 166, 549.

Gouliermis, D. A., Bestenlehner, J. M., Bradner, W., & Henning, T. 2010, A&A, 515, 56.

Hao, L., Spoon, H. W. W., Sloan, G. C., et al. 2005, ApJ, 625, 75.

Haser, S. M., Pauldrach, A. W. A., Lennon, D. J., et al. 1998, A&A, 330, 285.

Henize, K. G. 1956, ApJS, 2, 315.

Heydari-Malayeri, M., & Selier, R. 2010, A&A, 517, A39.

Higdon, S. J. U., Devost, D., Higdon, J. L., et al. 2004, PASP, 116, 975.

Hilditch, R. W., Howarth, I. D., & Harries, T. J. 2005, MNRAS, 357, 304.

Hony, S., Van Kerckhoven, C., Peeters, E., Tielens, A. G. G. M., Hudgins, D. M., & Allamandola, L. J. 2001, A&A, 370, 1030.

Houck, J. R., et al. 2004, ApJS, 154, 18.

Hudgins, D. M., & Allamandola, L. J. 1999, ApJ, 516, 41.

Hummer, D. G., Storey, P. J. 1987, MNRAS, 224, 801.

Hunt, L. K., Thuan, T. X., Izotov, Y. I., & Sauvage, M. 2010, ApJ, 712, 164.

Indebetouw, R., de Messières, G. E., Madden, S., et al. 2009, ApJ, 694, 84.

Keller, L. D., Sloan, G. C., Forrest, W. J., et al. 2008, ApJ, 684, 411.

Kennicutt, R. C. 1984, ApJ, 287, 116.

Lebouteiller, V., Brandl, B., Bernard-Salas, J., Devost, D., & Houck, J. R. 2007, ApJ,, 665, 390.

Lebouteiller, V., Bernard-Salas, J., Brandl, B., et al. 2008, ApJ, 680, 398.

Lebouteiller, V., Bernard-Salas, J., Sloan, G. C., & Barry, D. J. 2010, PASP, 122, 231.

Lebouteiller, V., Bernard-Salas, J., Whelan, D. G., et al. 2011, ApJ, 728, 45.

Lebouteiller, V., Sloan, G. C., Groenewegen, M. A. T., et al. 2012, A&A, 546, 94.

Leger, A., & Puget, J. L. 1984, A&A, 137, L5.

Li, A., & Draine, B. T. 2001, ApJ, 554, 778.

van Loon, J. T., Oliveira, J. M., Wood, P. R., et al. 2005, MNRAS, 364, L71.

Madden, S. C., Galliano, F., Jones, A. P., & Sauvage, M. 2006, A&A, 446, 877.

Massey, P., Parker, J. W., & Garmany, C. D. 1989, AJ, 98, 1305.

Massey, P., Puls, J., Pauldrach, A. W. A., et al. 2005 ApJ, 627, 477.

Myers, P. C., Adams, F. C., Chen, H., & Schaff, E. 1998, ApJ, 492,703.

Oliveira, V. A., Copetti, M. V. F., & Krabbe, A. C. 2008, A&A, 492, 463.

Parker, J. W. 1993, ApJ, 106, 560.

Peimbert, M., Peimbert, A., & Ruiz, M. T. 2000, ApJ, 541, 688.

Peeters, E., Hony, S., Van Kerckhoven, C., et al. 2002, A&A, 390, 1089.

Peeters, E., Spoon, H. W. W., & Tielens, A. G. G. M. 2004, ApJ, 613, 986.

Puget, J. L., & Léger, A. 1989, ARA&A, 27, 161.

Rieke, G. H., Young, E. T., Engelbracht, C. W., et al. 2004, ApJS, 154, 25.

Robberto, M., Bechwith, S. V. W., Panagia, N., et al. 2005, AJ, 129, 1534.

Robitaille, T. P., Whitney, B. A., Indebetouw, R., Wood, K., & Denzmore, P. 2006, ApJS, 167, 256.

Robitaille, T. P., Whitney, B. A., Indebetouw, R., & Wood, K. 2007, ApJS, 169, 328.

Roche, P. F., & Aitken, D. K. 1985, MNRAS, 215, 425.

Rubio, M., Contursi, A., Lequeux, J., et al. 2000, A&A, 359, 1139.

Russell, S. C., & Dopita, M. A. 1992, ApJ, 384, 508.

Sabbi, E., Sirianni, M., Nota, A., et al. 2007, AJ, 133, 44.

Sabbi, E., Sirianni, M., Nota, A., et al. 2008, AJ, 135, 173.

Sandstrom, K. M., Bolatto, A. D., Draine, B. T., Bot, C., & Stanimirović, S. 2010, ApJ, 715, 701.

Sandstrom, K. M., Bolatto, A. D., Bot, C., et al. 2012, ApJ, 744, 20.

Schutte, W. A., Tielens, A. G. G. M., & Allamandola, L. J. 1993, ApJ, 415, 397.

Sicilia-Aguilar, A., Hartmann, L. W., et al. 2007, ApJ, 659, 1637.

Simon, J. D., Bolatto, A. D., Whitney, B. A., et al. 2007, ApJ, 669, 327.

Sloan, G. C., & Price, S. D. 1995, ApJ, 451, 758.

Sloan, G. C., Keller, L. D., Forrest, W. J., et al. 2005, ApJ, 632, 956.

Smith, J. D. T., Draine, B. T., Dale, D. A., et al. 2007, ApJ, 656, 770.

Sturm, E., Schweitzer, M., Lutz, D., et al. 2005, ApJ, 629, 21.

Thuan, T. X. 2008, IAUS, 255, 348.

Tielens, A. G. G. M., Hony, S., van Kerckhoven, C., & Peeters, E. 1999, in *The Universe as Seen by ISO*, ed. P. Cox & M. F. Kessler (ESA SP-427; Nordwijk; ESA), 579.

Tielens, A. G. G. M. *The Physics and Chemistry of the Interstellar Medium.* Cambridge: Cambridge University Press, 2005.

Tsamis, Y. G., Barlow, M. J., Liu, X.-W., Danziger, I. J., & Storey, P. J. 2003, MNRAS, 338, 687.

Vermeij, R., Peeters, E., Tielens, A. G. G. M., & van der Hulst, J. M. 2002, A&A, 382, 1042.

Walborn, N. R., & Blades, J. C. 1986, ApJ, 304, L17.

Whelan, D. G., Johnson, K. E., Whitney, B. A., Indebetouw, R., & Wood, K. 2011, ApJ, 729, 111.

Wilke, K., Klaas, U., Lemke, D., et al. 2004, A&A, 414, 69.

Wisniewski, J. P., Bjorkman, K. S., Bjorkman, J. E., & Clampin, M. 2007, ApJ, 670, 1331.

Wu, Y., Charmandaris, V., Hao, L., et al. 2006, ApJ, 639, 157.

Table 1. Point Source Positions

RA (J2000)	Dec (J2000)	Designations			Source Identification
		This work	Lebouteiller et al. (2008)	Contursi et al. (2000)	
00h59m21.8s	-72d11m13.3s	PS1	–	–	
00h59m20.0s	-72d11m21.0s	PS2	9	I	
00h59m17.1s	-72d11m24.3s	PS3	13	–	
00h59m14.8s	-72d11m03.8s	PS4	8	H	1 class I YSO[b]
00h59m14.0s	-72d09m27.1s	PS5	–	G	N66C[a] ; 1 class II YSO[b]
00h59m12.3s	-72d09m58.7s	PS6	11	F	N66B[a] ; 1 class I YSO[b]
00h59m09.3s	-72d10m57.8s	PS7	5	E	N66A[a] ; 2 class I YSOs[b]
00h59m05.8s	-72d11m27.5s	PS8	7	D	KWBBE 200, a Be star
00h59m05.4s	-72d10m36.1s	PS9	6	C	N66[a] ; NGC 346
00h58m59.8s	-72d10m16.7s	PS10	–	–	
00h58m57.6s	-72d09m56.7s	PS11	–	–	
00h58m57.0s	-72d09m54.5s	PS12	10	A	
00h58m54.7s	-72d09m51.5s	PS13	–	–	
00h58m51.7s	-72d09m29.2s	PS14	–	–	

[a]HII regions from Henize (1956) ordered by brightness.

[b]YSO classifications are from Simon et al. (2007). Where multiple YSOs contribute to the point source flux, only class I YSOs are listed because they contribute the most to the point source flux.

Table 2. Slit Positions

RA	Dec	Designation[a]	Notes
00h59m49.99s	-72d13m00.1s	SLT1	sky position
00h59m42.00s	-72d11m09.9s	SLT2	sky position
00h59m21.62s	-72d11m17.2s	SLT3	
00h59m20.42s	-72d11m22.2s	SLT4	
00h59m17.30s	-72d11m25.1s	SLT5	
00h59m15.26s	-72d09m19.1s	SLT6	
00h59m14.69s	-72d11m03.1s	SLT7	
00h59m13.49s	-72d09m54.7s	SLT8	
00h59m12.29s	-72d09m58.3s	SLT9	
00h59m10.13s	-72d10m51.2s	SLT10	
00h59m09.24s	-72d10m57.0s	SLT11	
00h59m06.74s	-72d10m25.3s	SLT12	
00h59m05.98s	-72d11m26.9s	SLT13	
00h59m05.52s	-72d10m35.8s	SLT14	
00h58m59.11s	-72d10m23.2s	SLT15	
00h58m59.02s	-72d10m28.6s	SLT16	
00h58m58.32s	-72d09m50.0s	SLT17	
00h58m56.95s	-72d09m54.0s	SLT18	
00h58m52.42s	-72d09m24.1s	SLT19	

[a]The slits are labeled in order of decreasing slit centroid R.A. N.b. The slit labels do not necessarily correspond to the point source labels of the same number.

Table 3. Atomic, Ionic, and Molecular Hydrogen Line Measurements

Slit position	Type[a]	HI 6-5 7.46μm	[ArIII] 8.99μm	$H_2S(3)$ 9.67μm	[SIV] 10.51μm	$H_2S(2)$ 12.28μm	HI 7-6 12.37μm	[NeII] 12.81μm
				$\times10^{-21}$ W cm^{-2}				
PS1	ps	<0.47	<0.52	2.2±0.3	<0.11	0.77±0.12	<0.22	1.5±0.3
PS2	ps	3.3±0.7	<0.47	3.8±0.5	<0.41	1.6±0.2	<0.12	4.7±0.8
PS3	ps	0.8±0.2	<0.32	0.64±0.12	<0.18	0.41±0.08	<0.12	1.3±0.3
PS4	ps	<0.80	1.6±0.4	1.3±0.2	2.6±0.5	<0.91	<0.30	6.2±1.0
PS5	ps	<0.05	<0.09	5.4±1.1	<0.09	<0.056	<0.15	1.9±0.4
PS6	ps	<0.29	<0.09	<0.38	0.39±0.10	<0.097	<0.30	0.55±0.13
PS7	ps	<1.0	<0.80	0.54±0.11	<0.68	<0.52	<0.38	<0.70
PS8	ps	<0.40	<0.42	<0.59	<0.45	<0.11	<0.10	<0.38
PS9	ps	<0.67	<0.85	<2.1	<0.81	<0.68	<0.68	3.5±0.6
PS10	ps	<0.62	<0.17	1.3±0.2	<0.42	0.54±0.9	<0.052	1.3±0.3
PS11	ps	<0.45	<0.05	1.4±0.2	1.5±0.3	0.46±0.08	0.31±0.09	1.3±0.3
PS12	ps	<0.45	<0.38	0.67±0.13	<0.39	0.29±0.06	<0.032	0.45±0.11
PS13	ps	<0.37	<0.33	<0.37	<0.14	<0.35	<0.35	0.44±0.10
PS14	ps	<0.15	<0.21	1.2±0.2	<0.40	0.89±0.14	<0.037	0.98±0.21
SLT3	ee	<4.0	4.3±0.9	<0.52	41±5	<0.39	1.7±0.4	4.2±0.8
SLT4	ee	<2.9	1.2±2	<1.2	55±6	<0.79	3.7±0.7	4.2±0.7
SLT5	ee	<3.9	8.3±1.7	<4.7	60±0.7	<1.3	3.5±0.7	5.3±0.9
SLT6	ee	2.0±0.5	3.5±0.8	<0.26	54±6	<1.6	0.60±0.16	9.1±1.4
SLT8	ee	4.5±0.9	7.0±1.4	<0.57	72±8	<0.31	2.6±0.5	5.7±1.0
SLT9	ee	<0.82	9.6±1.9	<0.77	79±9	<0.82	<1.0	5.5±0.9
SLT10	ee	7.0±1.4	13±2	<0.40	94±10	<0.46	4.2±0.8	8.7±1.4
SLT11	ee	<2.3	19± 3	<1.4	104±11	<0.38	6.3±1.2	11±2
SLT12	ee	8.9±1.6	11±2	<0.38	87±9	<0.60	4.0±0.8	13±2
SLT13	ee	<8.3	10±2	<0.67	50±6	<0.19	2.7±0.6	5.8±1.0
SLT14	ee	<3.9	11±2	<0.32	106±11	1.3±0.2	2.6±0.5	9.8±1.5
SLT15	ee	8.4±1.6	11±2	<0.28	153±15	<0.27	2.7±0.6	5.9±1.0
SLT16 nod 1	ee	<11	18±3	<1.8	116±12	<1.3	6.4±1.2	8.0±1.3
SLT16 nod 2	ee	<19	11±2	<3.5	123±13	2.7±0.3	2.6±0.6	12±2
SLT17	ee	<0.40	9.6±1.9	<0.19	73±8	<0.27	2.5±0.5	5.2±0.9
SLT19	ee	<0.24	5.1±1.1	<0.10	16±2	<0.23	1.7±0.4	6.3±1.1

Table 3—Continued

Slit position	Type[a]	HI 6-5	[ArIII]	$H_2S(3)$	[SIV]	$H_2S(2)$	HI 7-6	[NeII]
		7.46μm	8.99μm	9.67μm	10.51μm	12.28μm	12.37μm	12.81μm
					$\times 10^{-21}$ W cm^{-2}			

[a] "Type" refers to the extraction method used to produce the spectrum: **ps** means an optimally extracted point source, and **ee** means extended emission extracted as a polynomial fit to the full-slit background.

Table 4. PAH and continuum measurements

Slit position	Type[a]	$PAH_{6.2\mu m}$	$PAH_{7.7\mu m}$	$PAH_{8.6\mu m}$	$PAH_{11.3\mu m}$	14μm continuum
			$\times10^{-20}$ W cm^{-2}			$\times10^{-20}$ W cm^{-2} μm^{-1}
PS1	ps	2.9±0.1	2.4±0.27	0.67±0.15	2.38±0.07	1.6
PS2	ps	7.4±0.3	18±2	3.5±0.5	6.2±0.4	5.9
PS3	ps	2.1±0.2	4.9±0.3	0.89±0.22	1.2±0.2	0.98
PS4	ps	2.9±0.2	7.4±1.3	1.4±0.4	3.3±0.3	2.1
PS5	ps	0.71±0.03	2.10±0.9	0.71±0.03	0.64±0.02	0.68
PS6	ps	0.28±0.02	0.96±0.04	0.21±0.05	0.52±0.01	0.65
PS7	ps	1.6±0.3	11±1	0.99±0.43	1.7±0.1	18
PS8	ps	2.5±0.4	6.3±1.1	1.2±0.3	2.26±0.06	3.0
PS9	ps	2.8±0.5	0.05±0.06	2.8±0.5	1.7±0.1	16
PS10	ps	1.61±0.05	3.2±0.3	0.59±0.08	1.50±0.03	1.2
PS11	ps	0.99±0.05	2.6±0.2	0.54±0.06	1.01±0.03	0.85
PS12	ps	0.81±0.08	8.1±0.7	1.0±0.2	1.45±0.07	3.5
PS13	ps	0.62±0.02	1.67±0.07	0.25±0.04	0.50±0.01	0.11
PS14	ps	1.20±0.07	3.5±0.2	0.48±0.08	2.1±0.1	0.60
SLT3	ee	2.6±0.3	3.4±0.34	1.1±0.2	1.3±0.3	2.2
SLT4	ee	3.1±0.31	18.6±0.9	0.81±0.30	2.2±0.2	4.8
SLT5	ee	4.3±0.4	17±2	1.9±0.6	2.9±0.4	5.3
SLT6	ee	5.2±0.3	11.4±0.8	3.3±0.3	4.2±0.3	4.3
SLT8	ee	3.7±0.3	7.3±0.56	1.9±0.4	2.5±0.5	3.8
SLT9	ee	2.4±0.4	10.1±0.9	0.51±0.35	1.4±0.2	4.9
SLT10	ee	6.7±0.4	19±1	2.6±0.8	5.5±0.6	8.6
SLT11	ee	3.5±0.3	19±1	1.7±0.5	2.5±0.2	9.7
SLT12	ee	8.0±0.5	17±2	3.0±0.8	7.4±0.7	9.1
SLT13	ee	2.3±0.3	5.2±0.7	1.1±0.3	1.3±0.1	4.4
SLT14	ee	4.0±0.5	21±2	1.9±0.6	3.3±0.3	7.9
SLT15	ee	3.0±0.2	6.9±0.69	1.2±0.4	1.0±0.2	8.6
SLT16 nod 1	ee	6.8±2.2	1.9±2.4	2.2±1.8	4.0±1.0	9.6
SLT16 nod 2	ee	4.9±2.0	9.6±4.0	2.3±1.9	4.4±1.0	12
SLT17	ee	1.9±0.1	4.6±0.3	0.60±0.14	1.20±0.07	1.7
SLT19	ee	3.8±1.0	9.5±0.3	2.6±0.2	2.02±0.06	2.3

Table 4—Continued

Slit position	Type[a]	$PAH_{6.2\mu m}$	$PAH_{7.7\mu m}$	$PAH_{8.6\mu m}$	$PAH_{11.3\mu m}$	14μm continuum
			$\times 10^{-20}$ W cm^{-2}			$\times 10^{-20}$ W cm^{-2} μm^{-1}

Note. — The PAH measurements here are those determined using PAHFIT. 15% errors are assumed on continuum fluxes.

[a] "Type" refers to the extraction method used to produce the spectrum: **ps** means an optimally extracted point source, and **ee** means extended emission extracted as a polynomial fit to the full-slit background.